

# Reviews of Geophysics

## REVIEW ARTICLE

10.1029/2019RG000655

### Key Points:

- The application of large eddy simulation technique to ocean mixed layer turbulence is reviewed
- Results from numerical investigations of material transport are summarized and synthesized
- Open questions and future research directions are discussed

**Correspondence to:**  
M. Chamecki,  
chamecki@ucla.edu

**Citation:**  
Chamecki, M., Chor, T., Yang, D., & Meneveau, C. (2019). Material transport in the ocean mixed layer: Recent developments enabled by large eddy simulations. *Reviews of Geophysics*, 57, 1338–1371.  
<https://doi.org/10.1029/2019RG000655>

Received 3 MAY 2019  
Accepted 23 SEP 2019  
Accepted article online 25 OCT 2019  
Published online 30 DEC 2019

## Material Transport in the Ocean Mixed Layer: Recent Developments Enabled by Large Eddy Simulations

Marcelo Chamecki<sup>1</sup> , Tomas Chor<sup>1</sup> , Di Yang<sup>2</sup>, and Charles Meneveau<sup>3</sup> 

<sup>1</sup>Department of Atmospheric and Oceanic Sciences, University of California, Los Angeles, CA, USA, <sup>2</sup>Department of Mechanical Engineering, University of Houston, Houston, TX, USA, <sup>3</sup>Department of Mechanical Engineering, Johns Hopkins University, Baltimore, MD, USA

**Abstract** Material transport in the ocean mixed layer (OML) is an important component of natural processes such as gas and nutrient exchanges. It is also important in the context of pollution (oil droplets, microplastics, etc.). Observational studies of small-scale three-dimensional turbulence in the OML are difficult, especially if one aims at a systematic coverage of relevant parameters and their effects, under controlled conditions. Numerical studies are also challenging due to the large-scale separation between the physical processes dominating transport in the horizontal and vertical directions. Despite this difficulty, the application of large eddy simulation (LES) to study OML turbulence and, more specifically, its effects on material transport has resulted in major advances in the field in recent years. In this paper we review the use of LES to study material transport within the OML and then summarize and synthesize the advances it has enabled in the past decade or so. In the first part we describe the LES technique and the most common approaches when applying it in OML material transport investigations. In the second part we review recent results on material transport obtained using LES and comment on implications.

**Plain Language Summary** The transport of materials in the ocean is a topic that has been attracting much interest in the last decades. Much of the importance of this topic lies in the fact that many of the materials considered impact ecosystem health and/or ocean-related industries. As examples we have pollutants (such as plastic and oil spills) and other natural substances like nutrients and phytoplankton. We focus on the upper part of the ocean, which is heavily impacted by the interaction with the atmosphere and, as a result, is particularly difficult to understand and predict. However, using increasingly more powerful computers, scientists have made significant advances over recent years. As a result, a large amount of new research has been made by different research groups investigating different aspects of the problem. In this review, we compile, summarize, and synthesize results produced by computer simulations into a coherent framework with the goal of better understanding the state of art of material transport. Finally, we conclude the paper with open research questions and directions for future research.

### 1. Introduction

Understanding and predicting transport and dispersion of materials in the ocean mixed layer (OML; sometimes also referred to as ocean surface boundary layer) is critical for a number of natural and human-made processes ranging from gas and nutrient exchanges to the fate of pollutants such as oil droplets and microplastics. The structure of the OML is such that large separation of scales exists between the dominant processes in the horizontal and vertical directions (Pedlosky, 1987, section 1.3). The large nearly two-dimensional mesoscale eddies and currents that dominate horizontal transport (Berloff et al., 2002; Chelton et al., 2011; Zhang et al., 2014) are well reproduced in regional models, and much progress has been made in understanding material transport at these scales. However, vertical transport is dominated by small-scale three-dimensional turbulence driven by various levels of wind shear, currents, waves, and buoyancy fluxes (Belcher et al., 2012; Large et al., 1994), and less is known about its effects on material transport. In the past decade attention has also been brought to the important presence of three-dimensional submesoscale flow features (McWilliams, 2016) that provide a more direct coupling between mesoscale and turbulence and play an important role in the transport of materials. The focus of the present review is on the small-scale three-dimensional turbulence and its consequences for transport and dispersion of materials in the OML.

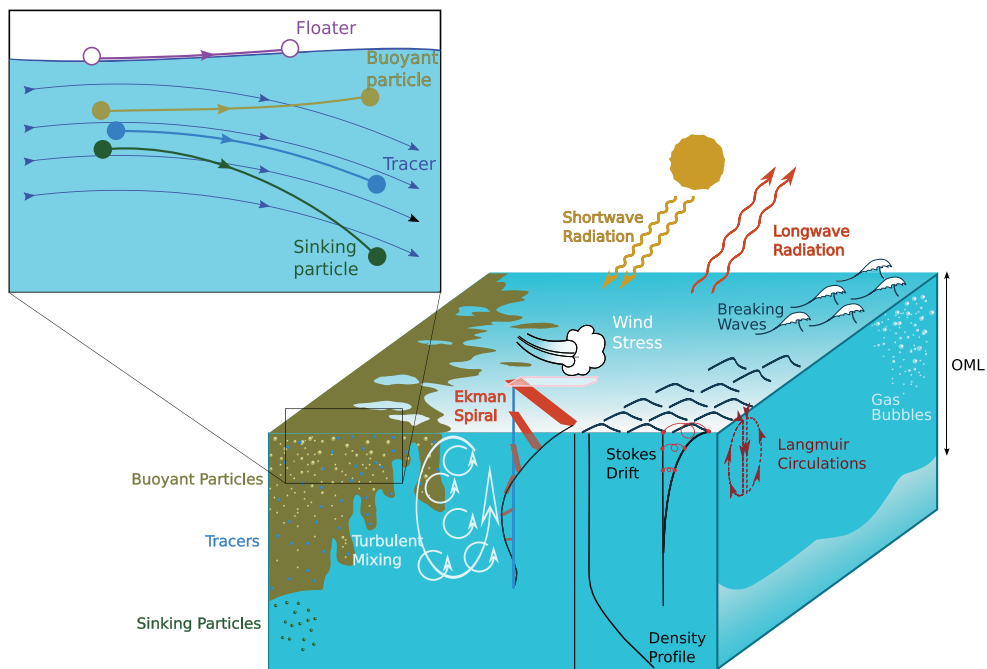


**Figure 1.** Schematic of relevant processes for the transport of material in the oceanic mixed layer (OML). Particles are primarily influenced by the wind shear (producing shear turbulence and an Ekman spiral in the presence of rotation), Stokes drift (subsequently causing Langmuir circulations by interacting with the shear turbulence), buoyancy fluxes at the surface (here indicated only by shortwave and longwave radiation, but in reality other processes such as evaporation and precipitation may also be important), breaking waves, and turbulent mixing due to OML dynamics. The inset shows the behaviors of four different particles subjected to the same flow: a surface floater, a buoyant particle, a neutral fluid tracer, and a sinking particle (see text for definitions).

Observational studies of three-dimensional turbulence in the OML are difficult and less common than in its atmospheric counterpart, the atmospheric boundary layer (ABL). As a consequence, most of the turbulence parameterizations required in regional models have been adapted from those developed for the ABL (Large et al., 1994). However, the presence of surface gravity waves modifies the turbulence dynamics in the OML, resulting in flows that have no counterpart in the ABL (D'Asaro, 2014; Sullivan & McWilliams, 2010). The rapid development and widespread use of the large eddy simulation (LES) technique have produced a revolution in our understanding of geophysical boundary layers. The technique, which was originally designed to study turbulence in the ABL (Deardorff, 1970b; Lilly, 1967), has made its way in the OML community in the mid-1990s (Skillingstad & Denbo, 1995; McWilliams et al., 1997), and a number of studies of vertical transport of materials followed in the past decade (Kukulka & Brunner, 2015; Liang et al., 2012; McWilliams & Sullivan, 2000; Noh et al., 2006; Skillingstad, 2000; Teixeira & Belcher, 2010). The use of LES has enabled fully three-dimensional high-fidelity simulations of complex turbulent flows in the OML and revealed a number of interesting features related to vertical mixing and its noticeable consequences to large-scale horizontal transport (specific references to be provided later in this paper in the appropriate contexts). However, most studies focused on a specific material (e.g., gas bubbles, biogenic particles, marine snow aggregates, microplastics, and oil droplets) and a limited set of forcing conditions (wind shear, buoyancy flux, waves, etc.; see Figure 1). The time is ripe for a synthesis of the existing knowledge that such simulations have enabled us to acquire, which should hopefully allow for a deeper understanding and help move the field forward.

At this point it is useful to establish some conventions in terms of the nomenclature to be used, as the lack of a common nomenclature in the literature is unhelpful. We will refer to solid particles, liquid droplets, and gas bubbles collectively as *particles*. By convention, *buoyant particles* are particles that are positively buoyant, having density smaller than that of sea water and a tendency to rise to the surface. We will use the terminology *sinking particles* for particles denser than sea water. The term *floaters* is reserved for buoyant particles that stay on the surface, and the term *tracer* is used to describe neutrally buoyant particles, whose motion tracks that of fluid parcels (see Figure 1). Finally, *active particles* are self-propelled particles that

are capable of producing their own motion in response to different environmental stimuli (e.g., plankton swimming).

This review paper consists of two main parts. Part 1 focuses on the LES technique, covering general modeling aspects and specific details relevant for its application to the OML. We focus on application of the technique to the filtered Navier-Stokes equations including relevant terms leading to, for example, the Craik-Leibovich (CL) equations. We discuss several different approaches to subgrid-scale (SGS) modeling that have been used by different groups. We also contrast the use of Eulerian and Lagrangian approaches to represent material transport and their respective advantages and disadvantages. We conclude Part 1 by discussing recently developed approaches for multiscale simulations of material transport.

Part 2 focuses on reviewing, organizing, and synthesizing the results and insights into flows and transport mechanisms obtained from LES in the past 10–15 years. Here we start by introducing the  $K$ -profile parameterization (KPP), since its basic structure has been used to frame a large portion of the OML research using LES. Next we discuss some of the important results that LES has enabled. Specifically, the following phenomena are discussed: preferential concentration of buoyant particles and floaters on the ocean surface, settling velocity of sinking particles, vertical mixing and resulting equilibrium profiles for buoyant particles, and effects of vertical distribution of material on horizontal transport and diffusion. We organize the discussions of these topics by categorizing them based on the dominant mechanisms of turbulence forcing (buoyancy, wind shear, and waves), and whenever possible attempt to recast available results within a unifying framework. We conclude the paper with a summary of the state of the science, pointing out open questions and future directions for investigation.

## 2. Tools

### 2.1. LES of OML Flows

#### 2.1.1. CL Equations

The vast majority of the numerical studies of OML turbulence has been performed in the context of wave-averaged dynamics. The underlying assumption is that the surface gravity waves represent the fastest component in the system and are not affected by the other components (turbulence and currents). Averaging the Navier-Stokes equations over a time scale  $T$  longer than the wave period results in a modified set of equations, typically referred to as the CL equations (Craik & Leibovich, 1976; Holm, 1996; Huang, 1979; Leibovich, 1977; Leibovich & Radhakrishnan, 1977):

$$\frac{\partial \mathbf{u}}{\partial t} + \mathbf{u} \cdot \nabla \mathbf{u} = -\nabla \pi + \left(1 - \frac{\rho}{\rho_0}\right) g \mathbf{e}_3 - 2\Omega \times \mathbf{u} + \nu \nabla^2 \mathbf{u} + \mathbf{u}_s \times \boldsymbol{\omega} - 2\Omega \times \mathbf{u}_s, \quad (1)$$

$$\nabla \cdot \mathbf{u} = 0. \quad (2)$$

Hereafter, we adopt a Cartesian coordinate systems  $\mathbf{x} = (x, y, z)$  with origin at the ocean surface and the positive vertical axis pointing upward (so  $z \leq 0$  within the domain of interest). In addition,  $\mathbf{u} = (u, v, w)$  is the Eulerian velocity field,  $\boldsymbol{\omega} = \nabla \times \mathbf{u}$  is the vorticity field,  $\mathbf{u}_s$  is the Stokes drift velocity,  $g$  is the gravitational acceleration,  $\mathbf{e}_3$  is the unit vector in the vertical direction,  $\rho_0$  is the reference density of sea water,  $\rho$  and  $\nu$  are the sea-water density and kinematic viscosity,  $\Omega$  is the angular velocity of Earth, and

$$\pi = \left( \frac{p}{\rho_0} + \frac{|\mathbf{u} + \mathbf{u}_s|^2}{2} - \frac{|\mathbf{u}|^2}{2} \right) \quad (3)$$

is a modified pressure with  $p$  being the dynamic pressure. Note that all the main flow variables in these equations (i.e.,  $\mathbf{u}$ ,  $\boldsymbol{\omega}$ ,  $\rho$ , and  $p$ ) are to be interpreted as time averages over a period  $T$ . The Stokes drift velocity is formally defined as

$$\mathbf{u}_s(z) = \frac{1}{T} \int_{-T/2}^{T/2} \left[ \int_t^T \mathbf{u}_w dt' \cdot \nabla \mathbf{u}_w(t') \right] dt, \quad (4)$$

where  $\mathbf{u}_w$  is the orbital velocity of the surface wave field (see review paper by van den Bremer & Breivik, 2018). The terms on the right-hand side of equation (1) are, in order, the (modified) pressure gradient force, buoyancy force due to sea water density variation, Coriolis force, viscous force, the vortex force (Craik & Leibovich, 1976), and Coriolis vortex force (Huang, 1979) resulting from the wave averaging procedure. Note

that these are not exact and are obtained based on a perturbation approach. For nearly irrotational waves with small slopes, the superposition of the Eulerian velocity and the Stokes drift is approximately equal the Lagrangian velocity  $\mathbf{u}_L = (\mathbf{u} + \mathbf{u}_s)$  (Leibovich, 1980). These equations are obtained with the assumption that the wave field is uniform in the horizontal directions, so that the resulting Stokes drift is only a function of  $z$ . As in the incompressible Navier-Stokes equations, incompressibility can be maintained if the modified pressure field is required to satisfy the Poisson equation obtained from the divergence of the CL equations. A particularly elegant derivation of the CL equations based on the generalized Lagrangian mean theory (Andrews & McIntyre, 1978) is presented by Leibovich (1980), and other modern derivations are given by Holm (1996) and McWilliams and Restrepo (1999).

Following the first LES studies based on the CL equations (McWilliams et al., 1997; Skillingstad & Denbo, 1995), it has become common practice to consider one single wave mode in the specification of the Stokes drift velocity profile (i.e., the dominant mode or an equivalent mode that would approximate some characteristic of the Stokes drift for the entire spectrum). For the simple case of a monochromatic wave train with angular frequency  $\omega = \sqrt{gk} \tanh(kH)$  (where  $k$  is the wave number and  $H$  is the water depth), this yields the classic profile

$$\mathbf{u}_s(z) = U_s \frac{\cosh[2k(z+H)]}{2\sinh^2(kH)} \mathbf{e}_w. \quad (5)$$

In equation (5),  $U_s = \omega ka^2$  is a measure of the magnitude of the Stokes drift (which is equal to the Stokes drift velocity at the surface for the deepwater waves),  $a$  is the wave amplitude, and  $\mathbf{e}_w$  is a unit vector in the direction of the wave propagation (Phillips, 1977). Note that for deepwater waves ( $kH > \pi$ , or ideally,  $kH \gg 1$ ; Dean & Dalrymple, 1991), equation (5) reduces to  $\mathbf{u}_s(z) = U_s \exp(2kz) \mathbf{e}_w$ . Despite the widespread use of the monochromatic wave Stokes drift, the vertical extent of Langmuir cells depends on the vertical profile of the Stokes drift velocity, which is different for a broadband spectrum. In particular, the use of the monochromatic wave to approximate the full spectrum underestimates the near-surface shear in  $\mathbf{u}_s$  and the magnitude of  $\mathbf{u}_s$  away from the surface due to larger penetration of longer waves (Breivik et al., 2014). For a known directional spectral density in the frequency domain,  $S(\omega, \vartheta)$  (typically parameterized based on field measurements), where  $\vartheta$  is the wave spreading angle with respect to the downwind direction, the Stokes drift  $\mathbf{u}_s$  for the deepwater case can be obtained by integrating the wave spectrum (Kenyon, 1969; McWilliams & Restrepo, 1999; Webb & Fox-Kemper, 2011),

$$\mathbf{u}_s(z) = \frac{2}{g} \int_0^\infty \int_0^{2\pi} \omega^3 S(\omega, \vartheta) \exp\left(\frac{2\omega^2}{g} z\right) (\cos \vartheta, \sin \vartheta, 0) d\vartheta d\omega. \quad (6)$$

The use of equation (6) requires the specification of the directional spectral density  $S(\omega, \vartheta)$ . This can be done by adopting empirical spectral density functions such as the Pierson-Moskowitz (Pierson & Moskowitz, 1964), Joint North Sea Wave Project (Hasselmann et al., 1976), or Donelan (Donelan et al., 1985) spectra or by using an independent wce model such as WAVEWATCH III (Tolman, 2009).

The final component to complete the set of CL equations is the density field, which is usually represented by a linear relationship to potential temperature ( $\theta$ ) and sometimes also salinity ( $S$ ) via  $\rho = \rho_0 [1 - \alpha_\theta (\theta - \theta_0) + \alpha_S (S - S_0)]$ , where  $\alpha_\theta$  and  $\alpha_S$  are the thermal expansion and haline contraction coefficients (Denbo & Skillingstad, 1996). The general approach is to write advection-diffusion equations for potential temperature and salinity and then use the simplified equation of state to obtain the density. For a generic scalar field  $\phi$  (that can be  $\theta$  and/or  $S$ ),

$$\frac{\partial \phi}{\partial t} + (\mathbf{u} + \mathbf{u}_s) \cdot \nabla \phi = D_\phi \nabla^2 \phi, \quad (7)$$

where  $D_\phi$  is the molecular diffusion coefficient and the Stokes-drift scalar advection is included (McWilliams & Restrepo, 1999). As in equation (1), here too  $\phi$ ,  $\theta$ , and  $S$  are time averaged over a period  $T$ . In most cases, sources and sinks of heat and salinity are specified via boundary conditions at the surface. As a final remark, the viscosity  $\nu$  and the diffusivity  $D_\phi$  appearing in equations (1) and (7) should also include the effects of the small scales of turbulence filtered out by the time averaging involved in the CL equations. In the present context, the inclusion of the turbulence component is not relevant, as it can be considered as part of the terms that arise from the spatial filtering formality of LES (see next subsection).

### 2.1.2. LES of CL Equations

From the perspective of LES, the great appeal of using the CL equations is the possibility of capturing the first-order accumulated effects of the waves on the turbulent flow (i.e., the Langmuir cells and their nonlinear interaction with three-dimensional turbulence) without the additional burden of resolving or explicitly representing the surface waves. In this wave-averaged framework, the flow features induced by the horizontal pressure gradients associated with the waves, as well as the effects of turbulence on the wave field, are neglected.

In LES, only the scales larger than a prescribed length scale  $\Delta$  (termed filter width) are resolved on the numerical grid. Reviews of LES can be found in Lesieur and Metais (1996), Meneveau and Katz (2000), and Sagaut (2006). Formally, the separation between resolved scales and SGSs is done by the convolution of the velocity field with a kernel  $G_\Delta(\mathbf{x})$  (Leonard, 1975). Thus, the resolved velocity field  $\tilde{\mathbf{u}}(\mathbf{x}, t)$  is obtained via

$$\tilde{\mathbf{u}}(\mathbf{x}, t) \equiv G_\Delta * \mathbf{u} = \int G_\Delta(\mathbf{x} - \mathbf{x}') \mathbf{u}(\mathbf{x}', t) d^3 \mathbf{x}' \quad (8)$$

and the formal decomposition is written as

$$\mathbf{u}(\mathbf{x}, t) = \tilde{\mathbf{u}}(\mathbf{x}, t) + \mathbf{u}_{\text{sgs}}(\mathbf{x}, t). \quad (9)$$

In equation (9),  $\mathbf{u}_{\text{sgs}}(\mathbf{x}, t)$  is the SGS velocity. The same decomposition applies to other variables of interest, such as density, pressure, potential temperature, salinity, and concentration of particles (see section 2.2.2).

Filtering the Craik-Lebovich equations (1) and (2), and neglecting the viscous term on the basis of large Reynolds number, yields

$$\frac{\partial \tilde{\mathbf{u}}}{\partial t} + \tilde{\mathbf{u}} \cdot \nabla \tilde{\mathbf{u}} = -\nabla \tilde{P} - \nabla \cdot \boldsymbol{\tau}^d + \left(1 - \frac{\tilde{\rho}}{\rho_0}\right) g \mathbf{e}_3 - 2\Omega \times (\tilde{\mathbf{u}} + \mathbf{u}_s) + \mathbf{u}_s \times \tilde{\boldsymbol{\omega}}, \quad (10)$$

$$\nabla \cdot \tilde{\mathbf{u}} = 0. \quad (11)$$

In equation (10),  $\boldsymbol{\tau} = (\tilde{\mathbf{u}}\tilde{\mathbf{u}} - \tilde{\mathbf{u}}\tilde{\mathbf{u}})$  is the SGS stress tensor, and  $\tilde{P} = \tilde{\pi} + \text{tr}(\boldsymbol{\tau})/3$  is a modified pressure. The SGS force (i.e., the divergence of the SGS stress tensor) represents the effects of the unresolved scales on the resolved velocity field and must be parameterized. For modeling purposes, one formally separates the SGS stress tensor into a deviatoric part ( $\boldsymbol{\tau}^d$ ) and an isotropic part proportional to the SGS kinetic energy  $e = (1/2)\text{tr}(\boldsymbol{\tau})$ . Thus,

$$\boldsymbol{\tau} = -\frac{2}{3} e \delta + \boldsymbol{\tau}^d, \quad (12)$$

where  $\delta$  is the Kronecker delta tensor. The deviatoric part is explicitly modeled, while the isotropic portion is included in the modified pressure  $\tilde{P}$ .

Finally, the filtered advection-diffusion equation for a generic scalar field (e.g., temperature and salinity) is given by

$$\frac{\partial \tilde{\phi}}{\partial t} + (\tilde{\mathbf{u}} + \mathbf{u}_s) \cdot \nabla \tilde{\phi} = -\nabla \cdot \boldsymbol{\pi}_\phi, \quad (13)$$

where  $\boldsymbol{\pi}_\phi = (\tilde{\mathbf{u}}\phi - \tilde{\mathbf{u}}\tilde{\phi})$  is the SGS scalar flux and the molecular diffusion has been neglected on the basis of large Péclet number. Closure of the filtered equations (10), (11), and (13) requires models for the SGS fluxes of momentum, heat, and salinity.

### 2.1.3. SGS Models

The vast majority of the LES studies of OML turbulence employ some variant of the eddy-viscosity model (Smagorinsky, 1963). In this approach, the deviatoric part of the SGS stress tensor is modeled as

$$\boldsymbol{\tau}^d = -2\nu_{\text{sgs}} \tilde{\mathbf{S}}, \quad (14)$$

where

$$\tilde{\mathbf{S}} = \frac{1}{2} (\nabla \tilde{\mathbf{u}} + \nabla \tilde{\mathbf{u}}^\top) \quad (15)$$

is the resolved strain-rate tensor. The rate of energy transfer between the resolved and SGS scales, often referred to as the SGS dissipation rate, is given by  $\Pi_\Delta = -(\boldsymbol{\tau}^d : \tilde{\mathbf{S}})$  (Lilly, 1967), being always positive for eddy-viscosity models. Eddy-viscosity models cannot represent the two-way instantaneous energy transfer across scales that occurs in turbulence but rather focus on correctly capturing the mean transfer from large to small scales. This turns out to be critical, as reproducing the correct rate of SGS dissipation is a sufficient condition to guarantee that the energy transfer across scales is properly represented in resolved scales much larger than the filter width (Meneveau, 1994; 2010).

The eddy viscosity (which in reality is an SGS viscosity, as it only represents the effects of scales smaller than the filter width) is then expressed as the product of a length scale and a velocity scale, and different models differ on the choices for these scales. In the Smagorinsky model (Smagorinsky, 1963), the length scale is proportional to the filter width  $\Delta$ , and the velocity scale is proportional to  $\Delta |\tilde{\mathbf{S}}|$ , where the magnitude of the strain-rate tensor is defined via  $|\tilde{\mathbf{S}}|^2 = 2(\tilde{\mathbf{S}} : \tilde{\mathbf{S}})$ . This choice results in

$$\nu_{\text{sgs}} = (C_s \Delta)^2 |\tilde{\mathbf{S}}|, \quad (16)$$

where  $C_s$  is the Smagorinsky coefficient. By assuming a sharp spectral cutoff filter in the inertial subrange (i.e., the intermediate range of scales where no production or dissipation of TKE occurs, and energy is only transferred across scales via inertial processes) and matching the SGS dissipation rate to the turbulence kinetic energy (TKE) dissipation rate (i.e., the rate of energy transfer across scales within the inertial subrange), Lilly (1967) linked  $C_s$  to the Kolmogorov constant and obtained the theoretical value  $C_s \approx 0.165$ .

The Smagorinsky model is seldom used in its original formulation. One of the issues is that, in the presence of mean shear, the resulting SGS viscosity is too large, leading to excessive dissipation of resolved TKE. Among the papers reviewed here, Taylor (2018) uses a modified version of equation (16) in which  $\tilde{\mathbf{S}}$  is replaced by its fluctuating component  $\tilde{\mathbf{S}}'$ , as proposed by Kaltenbach et al. (1994). Polton and Belcher (2007) replace  $(C_s \Delta)^2$  by  $(1 - Ri_f)^{1/2} \ell_m^2$ , where  $\ell_m$  is a length scale that depends on the local flux Richardson number  $Ri_f$  and the distance from the ocean surface  $z$ . Most other studies use more sophisticated versions of the eddy-viscosity closure discussed below.

The use of the original Smagorinsky model is also problematic in regions of the flow where the most energetic scales are not properly resolved. In simulations of the OML, this occurs mostly near the surface, where the local integral scale is reduced and becomes comparable to the filter width. In these conditions, the use of the dynamic model introduced by Germano et al. (1991) is advantageous. The basic idea behind the dynamic model is to leverage the information in the resolved scales to optimize the values of the Smagorinsky coefficient. The dynamic model is based on the Germano identity (Germano, 1992), given by

$$\mathbf{T} = \mathbf{L} + \hat{\boldsymbol{\tau}}. \quad (17)$$

Here,  $\hat{\mathbf{f}} \equiv G_{\rho\Delta} * \mathbf{f}$  represents a test filter applied on  $\mathbf{f}$  at scale  $\rho\Delta$  (with  $\rho > 1$ ), and  $\mathbf{L}$  and  $\mathbf{T}$  are the Leonard stress tensor and the SGS stress tensor resulting from the combination of the filters at scales  $\Delta$  and  $\rho\Delta$ , respectively. These two tensors are defined as

$$\mathbf{T} = \widehat{\mathbf{u}\mathbf{u}} - \widehat{\mathbf{u}\mathbf{u}}\widehat{\mathbf{u}\mathbf{u}} \quad \text{and} \quad \mathbf{L} = \widehat{\mathbf{u}\mathbf{u}} - \widehat{\mathbf{u}\mathbf{u}}\widehat{\mathbf{u}\mathbf{u}}. \quad (18)$$

The dynamic model approach exploits the fact that  $\mathbf{L}$  can be determined from the resolved velocity field  $\tilde{\mathbf{u}}$ , and that  $\boldsymbol{\tau}$  and  $\mathbf{T}$  can be written using the Smagorinsky closure (or any other closure, for that matter). If the Smagorinsky coefficient is assumed to be the same at both scales, the optimal coefficient that minimizes the mean square error of the Germano identity is given by (Lilly, 1992)

$$C_s^2 = \frac{\langle \mathbf{L} : \mathbf{M} \rangle}{\langle \mathbf{M} : \mathbf{M} \rangle}, \quad (19)$$

where

$$\mathbf{M} = 2\Delta^2 \left( \widehat{|\tilde{\mathbf{S}}|^2} - \rho^2 \widehat{|\tilde{\mathbf{S}}|^2} \right) \quad (20)$$

and the brackets indicate averaging performed over directions of statistical homogeneity (Germano et al., 1991) or along fluid parcel trajectories (Meneveau et al., 1996). The assumption that the coefficient is the

same at both scales relies on the assumption of scale-invariance of the nonlinear processes involved in the energy cascade, something that is only applicable in the inertial subrange (Meneveau & Katz, 2000). The scale-dependent version of the dynamic model relaxes the assumption of scale invariance by postulating a power law relationship between the Smagorinsky coefficient at different scales (Porté-Agel et al., 2000). Tejada-Martinez and Grosch (2007) and Özgökmen et al. (2012) use the standard dynamic model given by equation (19), while Yang et al. (2014) use the Lagrangian averaged scale-dependent version as described by Bou-Zeid et al. (2005), with the inclusion of the Stokes drift in the determination of Lagrangian trajectories.

An alternative approach to the Smagorinsky model first proposed by Deardorff (1973) is to use the SGS kinetic energy to obtain the velocity scale needed in the eddy-viscosity model, which can then be written as

$$v_{\text{sgs}} = C_e \ell e^{1/2}, \quad (21)$$

where  $\ell$  is a suitable length scale. This is usually referred to as the Deardorff 1.5 closure, and in most LES models,  $\ell = \Delta$  for neutral and unstable conditions and  $\ell = 0.76e^{1/2}/N$  ( $N$  being the Brunt-Vaisala frequency) for stable conditions (Deardorff, 1980). A prognostic equation for the SGS kinetic energy is included in the model, which requires closure of the dissipation and transport terms. The usual closure assumptions result in a prognostic equation of the form

$$\frac{\partial e}{\partial t} + (\tilde{\mathbf{u}} + \mathbf{u}_s) \cdot \nabla e = v_{\text{sgs}} (|\tilde{\mathbf{S}}|^2 + 2\tilde{\mathbf{S}} : \nabla \mathbf{u}_s) - \frac{1}{\rho_0} g \mathbf{e}_3 \cdot \boldsymbol{\pi}_\rho - C_e \frac{e^{3/2}}{\ell} + \nabla \cdot (2v_{\text{sgs}} \nabla e). \quad (22)$$

Note that two additional terms, representing advection of SGS kinetic energy by the Stokes drift and a production of SGS kinetic energy by the shear in the Stokes velocity, appear in equation (22) as a result of the wave-averaging procedure. The main advantage of including a prognostic equation for the SGS kinetic energy is that, contrary to the standard Smagorinsky model, no equilibrium between local production and local dissipation of TKE is assumed. This formulation (in this form or with some modifications) is used by a number of groups, including Skillingstad and Denbo (1995), McWilliams et al. (1997), and Noh et al. (2006).

The vast majority of the numerical studies of OML turbulence rely on some dynamic version of the Smagorinsky model or on Deardorff's 1.5 closure based on the prognostic equation for SGS TKE. Other than the exceptions already noted above, one additional exception is Mensa et al. (2015), who use a constant eddy viscosity model specifying different values for horizontal and vertical viscosity.

The most common approach to complete closure of the equations is to model the SGS heat/salinity flux using

$$\boldsymbol{\pi}_\phi = -\frac{v_{\text{sgs}}}{Sc_{\text{sgs}}} \nabla \tilde{\phi}, \quad (23)$$

where  $Sc_{\text{sgs}}$  is an SGS Schmidt number, which becomes an SGS Prandtl number  $Pr_{\text{sgs}}$  for the case  $\phi = \theta$ . The most commonly used approach to specify the SGS Prandtl number was proposed by Deardorff (1980) and consists of setting  $Pr_{\text{sgs}} = (1 + 2\ell/\Delta)^{-1}$ , yielding a constant value of 1/3 for neutral and unstable conditions with an increasing function that asymptotes to  $Pr_{\text{sgs}} = 1$  in strongly stable conditions. The reduction in  $Pr_{\text{sgs}}$  only impacts simulation results in the presence of strong stratification (Sullivan et al., 1994). Many studies simply set a constant value between 1/3 and 1 (Akan et al., 2013; Yang et al., 2014). Note that the dynamic approach based on test-filtering fields at scale  $\rho\Delta$  can also be used to determine a dynamic SGS Prandtl number during the simulation, as done in some closures used in studies of the ABL (Porté-Agel, 2004), but we are not aware of any OML study that employed this approach. At least in the case of the ABL, the evidence suggests that this approach does not have much advantage over combining the dynamic model for the momentum equations with a constant Prandtl number (Huang & Bou-Zeid, 2013).

The issue of SGS modeling is an important one, despite some general perception that LES solutions tend to be fairly insensitive to the choice of closure. It is true that mean fields (first-order statistics) away from boundaries are fairly insensitive to the specific details of the SGS model, especially if a fine resolution is adopted. However, second-order statistics such as the TKE can often be more sensitive. Perhaps the one example that can be used here is the comparison provided by Yang et al. (2015) with the results from McWilliams et al. (1997) for the simulation of Langmuir turbulence (see Figure 2). The two codes are very similar in terms of numerics, but the former used the Lagrangian scale-dependent Smagorinsky model while the latter used the Deardorff 1.5 closure. Simulation setup and grid resolution are identical and both studies handled inertial oscillations in a similar way, so that most of the differences observed in Figure 2 may be ascribed to the

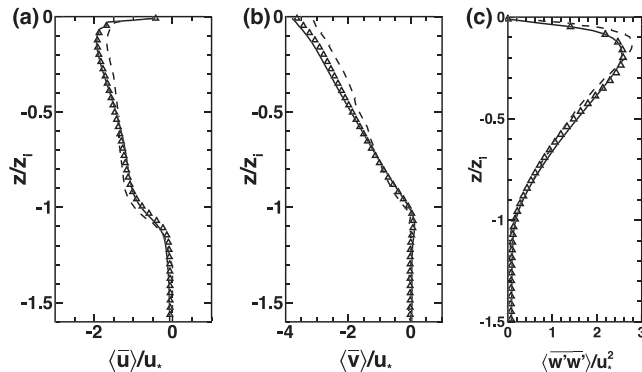


**Figure 2.** Comparison between simulations of McWilliams et al. (1997) (dashed lines) and Yang et al. (2015) (solid lines and symbols, with slightly different initial conditions) for the same Langmuir turbulence setup. Vertical profiles of (a) mean along-wind velocity  $\langle \bar{u} \rangle$  (b) mean cross-wind velocity  $\langle \bar{v} \rangle$ , and (c) vertical velocity variance  $\langle w'w' \rangle$ . Results normalized by the depth of the OML (here  $z_i$  instead of  $h$ ) and the friction velocity associated with the wind shear ( $u_*$ ). The main difference between the two simulations is the SGS model. Reproduced from Yang et al. (2015).

different SGS models. Note that the agreement is reasonably good, but differences are visible. For instance, the mean velocity profiles and the variance in vertical velocity are slightly different between the two simulations (particularly near the surface). In the absence of observational data or direct numerical simulation (DNS) results, one cannot conclude that one SGS model is superior to the other. But the comparison makes it clear that the choice of SGS model impacts the results. In the context of the present review, the differences in vertical velocity variance near the surface can be quite important for transport of buoyant materials.

More systematic comparisons between different SGS models have been performed for simulations of the ABL (e.g., Bou-Zeid et al., 2005; Mirocha et al., 2013), and there is no obvious reason for the conclusions not to apply to the OML. In general, different models lead to very significant differences in the structure of the resolved flow field (as evidenced, e.g., by differences in the energy spectrum), even when the agreement between low-order statistics is reasonably good (Bou-Zeid et al., 2005; Mirocha et al., 2013). Given that a lot of the emphasis of studies of Langmuir turbulence is placed on the structure of the Langmuir cells and its consequences for material transport, a comparison between different SGS models for OML turbulence would probably be a welcome addition to the literature.

## 2.2. Approaches to Simulate the Dispersed Phase

The focus of this review is on the transport of material in the OML, where material is broadly defined to include solid particles, liquid droplets, and gas bubbles. From a fundamental perspective, these materials are all viewed as a dispersed phase that is distributed within (and transported by) a carrier phase. The small volume fraction and mass loading associated with the dispersed phase in most applications of practical importance allow for a simple treatment in which the effects of the dispersed phase on the flow field can be neglected. This approach is usually referred to as one way coupling (Balachandar & Eaton, 2010). In some cases, however, feedbacks on the flow may be important, especially in the case of gas bubbles and buoyancy forces, requiring a two-way coupling approach.

The study of the motion of particles immersed in a turbulent flow field has a long history and its own many branches. The Maxey-Riley equation describing the forces experienced by small inertial particles (i.e., for particles with size much smaller than the Kolmogorov length scale  $\eta$ ) in a turbulent flow is given by Maxey and Riley (1983) and Auton et al. (1988). Here we start from a somewhat simplified version of this equation, in which the only forces acting are gravitational force, drag, virtual mass, and fluid stresses due to flow acceleration. For a spherical particle with diameter  $d_p$  and density  $\rho_p$ , the resulting particle acceleration is given by

$$\frac{dv_p}{dt} = -\frac{\mathbf{v}_p - \mathbf{u}}{\tau_p} + (1 - R) \mathbf{g} + R \frac{D\mathbf{u}}{Dt}, \quad (24)$$

where both the fluid velocity and acceleration must be evaluated at the particle position. In equation (24), the terms on the right-hand side are the drag force, the gravitational force combined with the virtual mass,

and the stresses due to flow acceleration. In addition,

$$\tau_p = \frac{1}{f(Re_p)} \frac{(\rho_p + \rho/2)d_p^2}{18\mu} \quad \text{and} \quad R = \frac{3\rho}{2\rho_p + \rho} \quad (25)$$

are the particle response time scale and the acceleration parameter, respectively. Finally,  $Re_p = |\mathbf{v}_p - \mathbf{u}|d_p/\nu$  is the particle Reynolds number based on the particle slip velocity, and  $f(Re_p) = (1 + 0.15Re_p^{2/3})$  is the Schiller-Naumann empirical correction to Stokes drag for  $Re_p < 800$  (Loth, 2008).

Equation (24) is usually the starting point in most studies of motion of inertial particles in turbulent flows (Balkovsky et al., 2001). In this equation, lift force, history force, Brownian motion, and the Faxén corrections were not included. Neglecting Brownian motion is consistent with the assumptions that molecular viscosity and diffusivity are negligible in equations (10) and (13), respectively. Inclusion of the history force and the Faxén corrections greatly complicates the problem, and both forces are usually small when the particle radius is small compared to the Kolmogorov scale (i.e.,  $d_p/(2\eta) \ll 1$ ). However, a recent DNS study of marine snow settling in homogeneous and isotropic turbulence by Guseva et al. (2016) has shown that when the particle density is only slightly larger than the fluid density, the history force greatly increases the time it takes for particles starting from rest to reach their terminal slip velocity, greatly reducing the overall settling rate in the flow. They also noted that the Faxén corrections were negligible in their study. Finally, Fraga and Stoesser (2016) have shown that the effect of the lift force can be important in segregating bubbles of different sizes when those are rising within a turbulent jet. Thus, perhaps with the exception of Brownian motion, more studies are needed before the limits of applicability of equation (24) can be clearly determined.

Even if these additional forces are neglected and the approximation given by equation (24) is accepted, one still has to evolve a separate set of differential equations for each particle's velocity. For small Stokes numbers (defined as the ratio between the particle response time and the turbulence time scale,  $St = \tau_p/\tau_t$ ), further simplification is possible, and equation (24) can be approximated as (Druzhinin, 1995; Ferry & Balachandar, 2001)

$$\mathbf{v}_p = \mathbf{u} + w_t \mathbf{e}_3 + \frac{w_t}{g} \frac{\mathrm{D}\mathbf{u}}{\mathrm{D}t}, \quad (26)$$

where we have introduced a generalized terminal slip velocity (Yang et al., 2016)

$$w_t = (R - 1) \tau_p g = \frac{1}{f(Re_p)} \frac{(\rho_p - \rho)gd_p^2}{18\mu}. \quad (27)$$

The main advantage of using the small Stokes number assumption is the diagnostic nature of equation (26), which no longer requires time integration of the equation set for particle velocity as in equation (24). Note that the terminal slip velocity between the particle and the fluid  $w_t$  is positive for buoyant particles and it is usually referred to as rise velocity  $w_r = w_t$ , while it is negative for sinking particles for which it is usually called settling velocity  $w_s = -w_t$ . The last term on the right-hand side of equation (26) is the leading-order inertial effect, being negligible in the limit  $St \ll 1$  (but even at  $St \approx 0.1$  inertial effects impact particle distribution by producing preferential concentration, e.g. see Coleman & Vassilicos, 2009).

For nonspherical particles, the drag coefficient and the terminal slip velocity will also depend on particle shape and surface roughness and the particle orientation in the flow (Bagheri & Bonadonna, 2016; Loth, 2008). In these cases, one can use measurements of terminal slip velocity and determine  $\tau_p$  from the first equality in equation (27). An alternative approach is to determine the terminal slip velocity using empirical expressions for the drag coefficient, such as the one proposed by Bagheri and Bonadonna (2016) that includes effects of particle orientation. In this case, an assumption about the distribution of particle orientation in the flow is needed. For gas bubbles and liquid droplets, the formulae proposed by Woolf and Thorpe (1991) and Zheng and Yapa (2000) are usually employed.

A list of typical values of terminal slip velocity and Stokes numbers for some of the particles of interest in studies of OML is presented in Table 1. For these estimates, we used three values of TKE dissipation rate in Langmuir turbulence with and without breaking waves estimated from Figure 10 in Sullivan et al. (2007):  $\epsilon \approx 5.5 \times 10^{-7} \text{ m}^2/\text{s}^3$  for the middle of the OML (estimated at about  $z/h \approx 0.5$ , where  $h < 0$  is the depth of the OML; see discussion in section 3),  $\epsilon \approx 5.3 \times 10^{-5} \text{ m}^2/\text{s}^3$  for the near surface of the OML without breaking

**Table 1**  
*Sample Properties of Some of the Particles of Interest*

Material	Diameter ( $\mu\text{m}$ )	$w_t$ (m/s)	$\tau_p$ (s)	Middle of OML		Sfc. (no wave breaking)		Sfc. (wave breaking)	
				St	Sv	St	Sv	St	Sv
Gas bubbles <sup>a</sup>	320	$3.0 \times 10^{-2}$	$3.1 \times 10^{-3}$	$2.2 \times 10^{-3}$	$3.4 \times 10^1$	$2.2 \times 10^{-2}$	$1.1 \times 10^1$	$9.9 \times 10^{-2}$	$5.2 \times 10^0$
	540	$6.0 \times 10^{-2}$	$6.1 \times 10^{-3}$	$4.4 \times 10^{-3}$	$6.9 \times 10^1$	$4.3 \times 10^{-2}$	$2.2 \times 10^1$	$2.0 \times 10^{-1}$	$1.0 \times 10^1$
	1,040	$1.2 \times 10^{-1}$	$1.2 \times 10^{-2}$	$8.8 \times 10^{-3}$	$1.4 \times 10^2$	$8.7 \times 10^{-2}$	$4.4 \times 10^1$	$3.9 \times 10^{-1}$	$2.1 \times 10^1$
Oil droplets <sup>b</sup>	100	$8.6 \times 10^{-4}$	$8.8 \times 10^{-5}$	$6.4 \times 10^{-5}$	$9.9 \times 10^{-1}$	$6.2 \times 10^{-4}$	$3.2 \times 10^{-1}$	$2.8 \times 10^{-3}$	$1.5 \times 10^{-1}$
	500	$1.4 \times 10^{-2}$	$1.4 \times 10^{-3}$	$1.0 \times 10^{-3}$	$1.6 \times 10^1$	$1.0 \times 10^{-2}$	$5.1 \times 10^0$	$4.5 \times 10^{-2}$	$2.4 \times 10^0$
	950	$3.1 \times 10^{-2}$	$3.2 \times 10^{-3}$	$2.3 \times 10^{-3}$	$3.6 \times 10^1$	$2.2 \times 10^{-2}$	$1.1 \times 10^1$	$1.0 \times 10^{-1}$	$5.3 \times 10^0$
Plastic debris <sup>c</sup>	—	$5.0 \times 10^{-3}$	$5.1 \times 10^{-4}$	$3.7 \times 10^{-4}$	$5.7 \times 10^0$	$3.6 \times 10^{-3}$	$1.8 \times 10^0$	$1.6 \times 10^{-2}$	$8.6 \times 10^{-1}$
	—	$3.5 \times 10^{-2}$	$3.6 \times 10^{-3}$	$2.6 \times 10^{-3}$	$4.0 \times 10^1$	$2.5 \times 10^{-2}$	$1.3 \times 10^1$	$1.2 \times 10^{-1}$	$6.0 \times 10^0$
Phytoplankton <sup>d</sup>	—	$5.8 \times 10^{-4}$	$5.9 \times 10^{-5}$	$4.3 \times 10^{-5}$	$6.7 \times 10^{-1}$	$4.2 \times 10^{-4}$	$2.1 \times 10^{-1}$	$1.9 \times 10^{-3}$	$1.0 \times 10^{-1}$
	—	$2.3 \times 10^{-3}$	$2.3 \times 10^{-4}$	$1.7 \times 10^{-4}$	$2.6 \times 10^0$	$1.7 \times 10^{-3}$	$8.4 \times 10^{-1}$	$7.6 \times 10^{-3}$	$4.0 \times 10^{-1}$

Note. Stokes numbers (St) and settling parameters ( $Sv = |w_t|/u_\eta$ ) are based on the Kolmogorov time and velocity scales ( $\tau_\eta = (\nu/\epsilon)^{1/2}$  and  $u_\eta = (\nu\epsilon)^{1/4}$ , respectively). Values of turbulence kinetic energy dissipation rate were estimated from Figure 10 in Sullivan et al. (2007) as discussed in the text. Values for  $w_t$  reported here are taken from the following references:

<sup>a</sup>Yang et al. (2016). <sup>b</sup>Chor et al. (2018b). <sup>c</sup>Kukulka et al. (2012). <sup>d</sup>Noh et al. (2006).

waves (estimated here from an LES near the surface at a depth of  $z/h \approx 0.008$ ), and  $\epsilon \approx 1.1 \times 10^{-3} \text{ m}^2/\text{s}^3$  for the near surface of the OML with breaking waves (also estimated at  $z/h \approx 0.008$ ). We consider the former two as reasonably large dissipation rates in the absence of breaking waves and the latter as a reasonable upper bound on possible values encountered in the OML. Thus, the estimated values of  $St_\eta = \tau_p/\tau_\eta$  (with  $\tau_\eta = \sqrt{\nu/\epsilon}$ ) can be considered as fairly large values. Clearly, inertial effects are negligible in the bulk of the OML for all particles listed. It is only near the surface of the OML and in the presence of wave breaking that inertial effects may play a noticeable role in the transport of large gas bubbles, oil droplets, and plastic debris (assessment of importance of inertial effects should be based on the criterion  $St_\eta \geq 0.1$ —see Table 1 for sample values). As a side note, the three values of dissipation quoted above correspond to Kolmogorov length scales  $\eta = 1,200, 385$ , and  $180 \mu\text{m}$ , and consequently, the assumption  $d_p/(2\eta) \ll 1$  for the validity of the Maxey-Riley equation is not always satisfied for the particles listed in Table 1.

The effects of turbulence on the terminal slip velocity of inertial particles have attracted considerable attention, since the DNS results of Wang and Maxey (1993) showed that turbulence could significantly increase the average terminal velocity of inertial particles compared to their slip velocity in still fluid (i.e.,  $(|w_{t,\text{eff}}| - |w_t|) > 1$ , where  $w_{t,\text{eff}}$  is the effective particle slip velocity in a turbulent flow and  $w_t$  is the particle terminal slip velocity in still fluid as defined in equation (27)). Wang and Maxey (1993) showed that settling particles tend to oversample regions of downward velocity (known as the “fast-tracking” or “preferential-sweeping” mechanism), leading to significant increases in the mean settling velocity. Similarly, one would expect rising particles to preferentially sample upward velocities. On the other hand, fast-falling particles may spend more time on upward moving flow, a mechanism usually referred to as “loitering” (Nielsen, 1993). The dominant mechanism and the magnitude of the effects depend on several dimensionless parameters, and only a small portion of this multidimensional parameter space has been properly sampled. Nevertheless, it seems clear that the effect is only important for  $St_\eta \geq 0.1$ , and its magnitude and direction (i.e., increasing or reducing terminal slip velocity) depend both on  $St_\eta$  and the settling parameter  $Sv_\eta = |w_t|/u_\eta$  (where  $u_\eta = (\nu\epsilon)^{1/4}$  is the Kolmogorov velocity scale). A combination of laboratory experiments and numerical simulations presented by Good et al. (2014) maps a portion of the parameter space (see Figure 3), and it can be considered a summary of our current understanding of this phenomenon. Note that in the figure, the magnitude of the increase represented by  $\beta_{\text{turb}} = (w_{t,\text{eff}} - w_t)/W$  scales with a characteristic turbulence velocity scale  $W$  (to be more precisely defined in section 4.1). The main conclusion from Figure 3 is that for turbulence to have a significant impact on the average terminal velocity, both  $St_\eta$  and  $Sv_\eta$  must be of order 1.

Although the results in Figure 3 are for low Reynolds number turbulence and heavy particles ( $\rho_p/\rho \gg 1$ ), we use them in interpreting the potential for inertial terminal velocity changes in the OML. On Figure 3

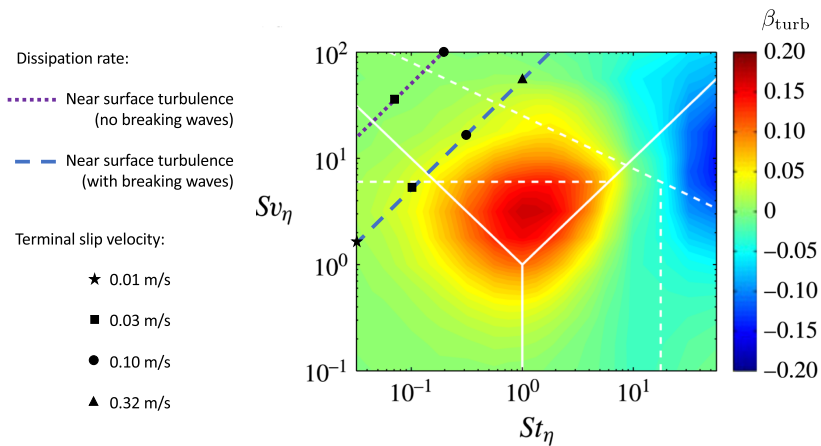


**Figure 3.** Isocontours of  $\beta_{\text{turb}} = (w_{t,\text{eff}} - w_t)/W$  on the  $St_\eta$ – $Sv_\eta$  plane obtained from direct numerical simulation of homogeneous isotropic turbulence at  $Re_\lambda = 140$ . Here  $W$  is a turbulence velocity scale. Figure adapted from Good et al. (2014).

we plot two near-surface values of TKE dissipation rate in Langmuir turbulence, as estimated from Figure 10 in Sullivan et al. (2007). We remark that values of dissipation in the middle of the OML are too small to appear within the plotted range in this figure. Note that a pair of values for  $v$  and  $\epsilon$  establishes a line in this parameter space and the value of  $w_t$  determines the position along that line. Thus, changing particle size changes only the location along the line. Note that for our estimated values for the top of the OML in the presence of breaking waves, which is the condition most likely to lead to relevant changes in the slip velocity,  $\beta_{\text{turb}}$  is still small:  $\beta_{\text{turb}} \approx 0.05$ . The conclusion from this analysis is that, based on the results from Good et al. (2014), the small values of TKE dissipation rate in the OML lead to small values of  $\beta_{\text{turb}}$ . Thus, the evidence seems to point to these effects not being important in general, with the possible exception of cases in the presence of strong breaking waves. Note also that even for very small values of  $\beta_{\text{turb}}$ , the relative increase in terminal velocity  $(w_{t,\text{eff}} - w_t)/w_t = \beta_{\text{turb}} W/w_t$  can be quite large if  $W/w_t$  is large (even with a small  $\beta_{\text{turb}}$ ). However, for most applications, this increase is likely to be unimportant, since  $W/w_t \gg 1$  implies that the actual value  $w_t$  is quite small (see further discussion in section 4.1).

In the context of LES, equation (26) is filtered, and the magnitude of the last term after filtering is proportional to  $St_\Delta = \tau_p/\tau_\Delta$ , where  $\tau_\Delta$  is a time scale for the smallest resolved eddies in the LES (Balachandar & Eaton, 2010). For closures using the Smagorinsky model,  $\tau_\Delta = |\tilde{\mathbf{S}}|^{-1}$  seems to be a natural choice, while  $\tau_\Delta = e^{1/2}/\ell$  is more appropriate with the use of Deardorff's 1.5 closure. Note that when  $w_t$  is used from empirical correlations as is often the case, an approximate response time scale can be obtained from equation (27) for the purpose of estimating  $St_\Delta$ . For the resolutions currently used in LES of OML, inertial effects are negligible for any reasonable particle size, and the inclusion of the inertial term on the right-hand side of (26) is not necessary. The same is true about the lift force (Yang et al., 2016). Thus, if these effects are to be incorporated into current LES studies, this must be done via new SGS models.

### 2.2.1. Lagrangian Approach

The vast majority of the studies of material transport in the OML adopt a Lagrangian approach. In fact, most of the first papers studying material transport in the OML considered only floater particles, which were then used as a visualization tool to illustrate features of surface convergence, one of the most recognizable characteristics of Langmuir turbulence (McWilliams et al., 1997; McWilliams & Sullivan, 2000; Skillingstad, 2000; Skillingstad & Denbo, 1995). The study by Noh et al. (2006) on sinking particles and by Kukulka et al. (2012) on buoyant particles are the first studies to go beyond floaters and to seek some quantitative analysis of their behaviors.

In the Lagrangian approach, the flow is seeded with a large number of particles whose position  $\mathbf{x}_p$  is evolved according to

$$\frac{d\mathbf{x}_p}{dt} = \mathbf{v}_p, \quad (28)$$

where  $\mathbf{v}_p$  is the particle velocity. All studies reviewed here are based on the limit  $St \ll 1$ . In this case, the inertial term on the right-hand side of equation (26) is negligible and the particle velocity is given by

$$\mathbf{v}_p = \tilde{\mathbf{u}}(\mathbf{x}_p) + \mathbf{u}_{sgs}(\mathbf{x}_p) + \mathbf{u}_s(\mathbf{x}_p) + w_t \mathbf{e}_3. \quad (29)$$

Here  $\tilde{\mathbf{u}}(\mathbf{x}_p)$  is the resolved velocity field at the particle location (usually obtained from the LES fields via interpolation from the grid-scale velocity), and  $\mathbf{u}_{sgs}$  is the contribution of the SGSs to the particle velocity. Because individual particle trajectories are determined independently, the SGS velocity vector is needed for each particle and SGS modeling has to be handled in a different framework from that used for the continuum equations in section 2.1. In LES models for the ABL, the SGS velocity has been represented using a Lagrangian stochastic model (LSM) proposed by Weil et al. (2004). In this framework, which is based on the model constructed by Thomson (1987), the SGS velocity is obtained from a stochastic differential equation containing two main parts, a drift part constrained by the LES fields and a stochastic part. Lagrangian studies of particles in the OML often neglect the SGS component without justification. It seems reasonable to neglect this component for floaters (and many studies focused only on floaters) since their motion is determined by the horizontal components of velocity, which are well resolved at the surface due to the free-slip boundary condition. However, neglecting  $\mathbf{u}_{sgs}$  seems less justified for buoyant, sinking, and tracer particles, whose motion is strongly impacted by vertical velocity fluctuations that tend to be poorly resolved near the surface (due to the no-penetration boundary condition). Noh et al. (2006) argue that the SGS kinetic energy is smaller than the resolved portion of the TKE, thus rendering the SGS velocity portion negligible. Nevertheless, the vertical component of the SGS velocity in the OML need not be negligible and cannot be neglected without supporting results. The work by Liang et al. (2018) on buoyant particles seems to be the first exception, in which the SGS velocity is estimated from a random displacement model (a simpler version of the full LSM in which only the random component is included). More recently, Kukulka and Veron (2019) implemented a full LSM for the SGS velocity component in the simulation of tracer particles and showed that the inclusion of the SGS component does have an important impact on the tracer statistics. Most notably, in their simulation, neglecting the SGS contribution reduced the decay in the Lagrangian autocorrelation functions, causing an overestimation of the Lagrangian integral time scales by 10–20%. The authors did not report the effects on particle dispersion, but one would expect a similar overestimation of the turbulent diffusivities.

In principle the Lagrangian approach is the most natural choice to treat material transport, in particular if there is interest in predicting individual particle interactions. The Lagrangian approach is also the ideal approach to handle highly inertial particles with  $St > 1$  (Balachandar & Eaton, 2010), but this limit does not seem relevant in OML simulations. One advantage of the Lagrangian approach in studies of material transport in the ocean is that it allows easy computation of connectivity between different regions (Mitarai et al., 2009). The Lagrangian approach is algorithmically uncomplicated to implement (Liang et al., 2011) and easily parallelizable. The main disadvantage of the Lagrangian approach lies in the computational cost of simulating the enormous number of particles necessary to produce statistically converged results for the entire three-dimensional space. This issue becomes even more severe when flow features induce preferential concentration of particles in small regions of the domain (see section 4.2). The notion of “representative particles” (simulating only a subset of the actual particles and then rescaling the results by the actual number density) is helpful in avoiding to have to simulate the actual number of particles (e.g., see Loth, 2010, p. 191). But still, the number of representative particles required to obtain converged statistics is often very large.

### 2.2.2. Eulerian Approach

In the Eulerian approach the dispersed phase is treated via continuous particle concentration and velocity fields, which then satisfy mass and momentum conservation principles (Crowe et al., 1998). This is the most direct approach for predicting particle concentration distribution since unlike Lagrangian methods, no subsequent averaging is required. The main fundamental limitation of the Eulerian approach arises for particles with  $St > 1$  (see Figure 1 in Balachandar & Eaton, 2010) for which particle trajectories can cross and a unique particle velocity vector field may be difficult to define, where a separate momentum equation for the particle field is needed. For particles with small Stokes number in the dilute regime, the much simpler equilibrium Eulerian approach is often used. In this approach, mass conservation is used to obtain an equation for the evolution of the concentration field, and the particle velocity is diagnosed from a formulation based on equation (26), without the need for evolving the dispersed phase momentum equations. In applications in the dilute regime based on the equilibrium Eulerian approach, the filtered equation can be written as

$$\frac{\partial \tilde{C}}{\partial t} + \nabla \cdot (\tilde{\mathbf{v}} \tilde{C}) = -\nabla \cdot \boldsymbol{\pi}_c, \quad (30)$$

where  $C$  is the particle mass concentration field,  $\tilde{\mathbf{v}}$  is the velocity of the particle field, and  $\boldsymbol{\pi}_c = \tilde{\mathbf{v}}\tilde{C} - \tilde{\mathbf{C}}\tilde{\mathbf{v}}$  is the SGS flux of particle mass concentration. Typically, the conservation equation is used for monodispersed particles, and the treatment of polydispersed flows encompasses several concentration fields  $C_i$  representing different size (or slip velocity) bins. Equations for the different size bins can be coupled representing changes in size due breakup, coalescence, gas diffusion, and so forth. One example of application of this coupled polydispersed approach is the study of gas bubbles by Liang et al. (2011). For oil droplets, a recent application is found in Aiyer et al. (2019).

In the Eulerian approach, only the resolved particle velocity is needed, as the unresolved component appears in the form of an SGS flux term. In the Eulerian equilibrium approach, the resolved particle velocity is given by (Yang et al., 2014)

$$\tilde{\mathbf{v}} = \tilde{\mathbf{u}} + w_t \mathbf{e}_3 + \frac{w_t}{g} \left( \frac{D\tilde{\mathbf{u}}}{Dt} + \nabla \cdot \boldsymbol{\tau} \right) + \mathbf{u}_s, \quad (31)$$

where  $D\tilde{\mathbf{u}}/Dt = \partial\tilde{\mathbf{u}}/\partial t + \tilde{\mathbf{u}} \cdot \nabla \tilde{\mathbf{u}}$ . The term with the divergence of the SGS stress tensor is usually neglected based on the smallness of the SGS energy and the small values of  $St_A$  in most LES applications (Shotorban & Balachandar, 2007). We note that the inertial term on the right-hand side of equation (31) is usually neglected in OML simulations and the studies that do include it (Yang et al., 2014, 2015) do not quantify its importance.

One advantage of the Eulerian approach is that the SGS term can be handled as an extension of the models adopted for the potential temperature and salinity fields using equation (23). This approach is used by Yang et al. (2014), who adopts a constant Schmidt number  $Sc_{sgs} = 0.8$  for all buoyant particles considered. As a final note, we also point out that some studies (Liang et al., 2012, 2014; Yang et al., 2015) include a feedback of the particle field on the velocity field via Boussinesq approximation by adding a buoyant force given by

$$\mathbf{F}_{bc} = \left( 1 - \frac{\rho_p}{\rho} \right) \frac{\tilde{C}}{\rho} g \mathbf{e}_3 \quad (32)$$

to the right-hand side of the filtered CL equation (10). This effect is clearly important in the case of gas bubbles (Liang et al., 2012).

### 2.3. Multiscale Approaches

One limitation of LES studies is that the high computational cost associated with the fine resolution required for these simulations has prevented the use of very large domains necessary to represent the mesoscale and submesoscale features that control horizontal transport of material. Only recently, LES has been applied on a domain large enough ( $20 \text{ km} \times 20 \text{ km}$ ) to capture the interaction between Langmuir turbulence and a submesoscale frontal system, as in the impressive simulation by Hamlington et al. (2014). Even though such large simulations are possible, they remain costly, and as a result it is not yet practical to run enough simulations of this size to explore relevant parameter spaces. If the goal is to simulate and quantify material transport covering a range of relevant conditions, alternative multiscale approaches that do not explicitly resolve the coupling between all scales can be an attractive alternative.

Malecha et al. (2014) developed a multiscale algorithm based on asymptotic expansions of the CL equations using multiple space and time scales. Their approach leads to coupled partial differential equations governing phenomena at different scales, and the computational advantage comes from using small representative subdomains to simulate the small-scale dynamics. In the atmospheric sciences community, the use of a second numerical model to represent small-scale processes within a large-scale model is known as superparameterization, and it has been used to improve cloud physics processes in mesoscale and global circulation models (Khairoutdinov et al., 2005; Majda, 2007) and to represent anisotropic turbulence in geophysical flows (Grooms & Majda, 2013). In this sense, the approach proposed by Malecha et al. (2014) is quite similar to superparameterization. Even though Malecha et al. (2014) did not consider the transport of materials, their approach can be easily extended to this application.

Another approach is the Extended Nonperiodic Domain LES for Scalars (ENDLESS), which was originally developed as a multiscale approach for oil transport (Chen et al., 2016b). In ENDLESS, OML turbulence (equations (10), (11), and (13)) is simulated on a small horizontal domain while the material plume (equation (30)) is simulated over an effectively large extended domain (Figure 4). In particular, this approach permits the superposition of large-scale divergence-free two-dimensional motions on the material advection, providing a framework for coupling the effects of turbulence from LES and submesoscale

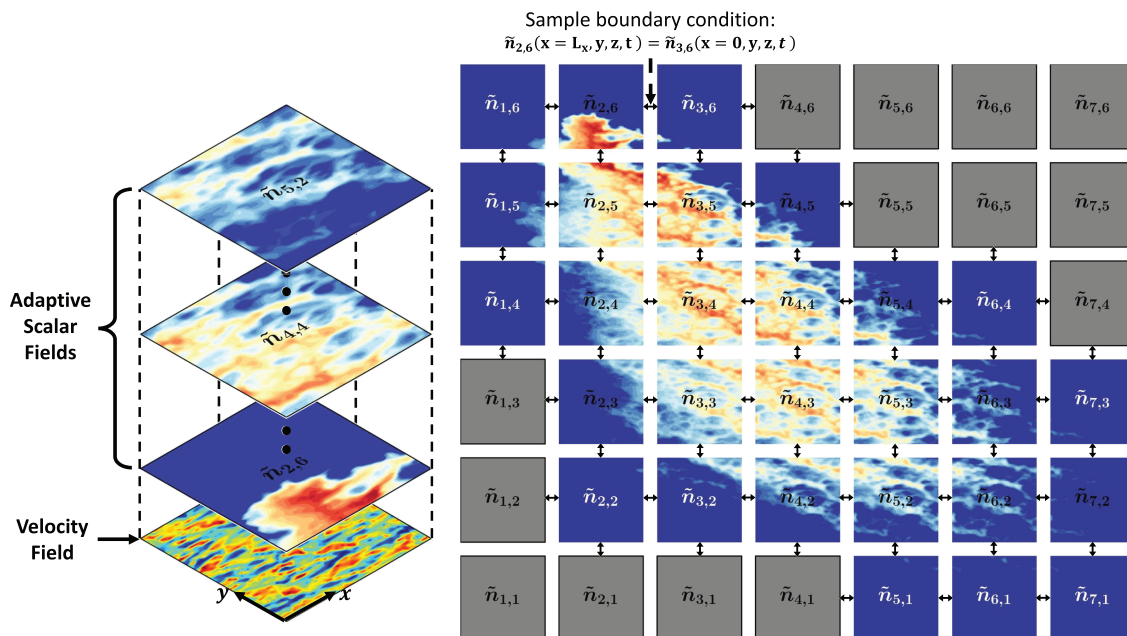


**Figure 4.** Extended Nonperiodic Domain large eddy simulation for Scalars multiscale approach developed to simulate oil dispersion in the ocean mixed layer. Several scalar fields of mass concentration are transported by the same velocity field (left panel) and interconnected via boundary conditions to cover a plume spreading over a large horizontal area (right panel). The colors indicate surface concentration of oil droplets, and the gray patches represent scalar fields inactive in the current time step. Reproduced from Chen et al. (2016b) with permission.

and mesoscale features from regional circulation models on material transport. Contrary to the approach by Malecha et al. (2014), the superposition approach in ENDLESS requires the dynamic interactions between large-scale eddies and small-scale turbulence to be disregarded (this actually leads to very significant computational savings). ENDLESS has been used by Chen et al. (2018) to study large oil plumes from deepwater blowouts and in a Lagrangian formulation by Liang et al. (2018) to study shear dispersion in the OML.

### 3. Applications of LES to OML Turbulence Without Material Transport

The use of LES has enabled major advances in our understanding of turbulence in the OML even without material transport considerations. While a complete review of the topic is outside of the scope of this paper, we briefly mention a few important results that demonstrate the range of applications in which the LES technique has been used and sets the stage for the discussion of material transport in the next sections. Reviews of other aspects of LES applied to the OML are included in D'Asaro (2014), Sullivan and McWilliams (2010), and van den Bremer and Breivik (2018).

Throughout this paper we denote the OML depth  $h$  as a negative number, as it corresponds to a specific position along the  $z$  axis. While most studies define it as a positive number, both definitions are common in the literature. In places where the OML depth is used as a scaling parameter, we use  $|h|$  to maintain consistency.

The first LES studies of OML turbulence using the filtered CL equations by Skyllingstad and Denbo (1995) demonstrated that this framework was indeed capable of generating Langmuir circulations and that their presence enhanced near-surface turbulence. McWilliams et al. (1997) included the Coriolis-Stokes force omitted by Skyllingstad and Denbo (1995) in their model and explored in detail the differences between the OML driven by wind shear alone and the one driven by wind shear and wave forcing (hereafter called “Langmuir turbulence”). Their results showed that Langmuir turbulence is characterized by enhanced levels of turbulence and momentum flux within the entire OML, resulting in reduced shear in mean velocity profiles. They also showed a very large increase in the vertical velocity variance (about fivefold increase), which carries enormous implications for vertical material transport, and introduced the turbulent Langmuir number

$$La_t = (u_*/U_s)^{1/2} \quad (33)$$

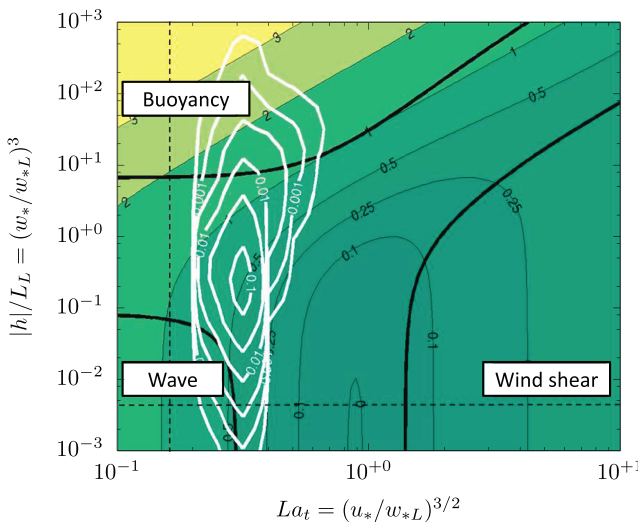


**Figure 5.** Regime diagram for turbulence in the ocean mixed layer. Colored contours show the logarithm of the normalized turbulence kinetic energy dissipation rate  $\log_{10}(\epsilon|h|/u_*^3)$ . Thick solid lines divide the regime diagram into regions dominated by one forcing (buoyancy-driven, wind shear-driven, and wave-driven ocean mixed layer). White contours show the joint probability distribution function of  $La_t$  and  $|h|/L_L$  for the Southern Ocean winter. Figure adapted from original by Belcher et al. (2012).

1970a), and  $w_{*L} = (U_s u_*^2)^{1/3}$  for Langmuir turbulence (Harcourt & D'Asaro, 2008). This is equivalent to replacing the Hoennikker number by  $|h|/L_L = (w_*/w_{*L})^3$ . Belcher et al. (2012) also obtained an estimate for the TKE dissipation rate  $\epsilon$  as a linear combination of the three production mechanisms and showed that, for the Southern Ocean winter, the joint probability distribution function of  $La_t$  and  $|h|/L_L$  peaked in a regime where wave and buoyancy forcing were both important.

Sullivan et al. (2007) increased the realism of LES models of the OML by including a Stokes drift profile calculated from a broadband wave spectrum and a stochastic model for wave breaking. The latter is modeled by representing the effects of discrete wave-breaking events using an additional term on the right-hand side of equation (10) and an SGS energy generation rate on the right-hand side of equation (22). In their simulations, the inclusion of wave breaking caused a large increase in total TKE, but the vast majority (if not all) of this increase was in the SGS component of the TKE. Harcourt and D'Asaro (2008) explored a wide range of oceanic conditions in which the wind stress and wave spectrum were obtained from different combinations of mean wind speed and wave age. The authors show that turbulence produced by Stokes drift profiles obtained from a broadband wave spectrum can yield different scaling results from that produced by monochromatic waves, highlighting the importance of using the full wave spectrum in future studies (this is particularly important for comparison with observations, in which wind and waves are not necessarily in equilibrium). They also defined a surface layer Langmuir number, which is a better predictor for the magnitude of vertical velocity fluctuations and TKE in a range of oceanic conditions.

Van Roekel et al. (2012) studied a series of cases in which wind and waves were not aligned, introducing a misalignment angle  $\varpi$ . They found that the misalignment reduced the intensity of vertical velocity fluctuations and that this reduction could be estimated by projecting the friction velocity into the direction aligned with the Langmuir cells and defining a “projected” turbulent Langmuir number

$$La_{t,proj}^2 = \frac{\cos(\varphi)}{\cos(\varpi - \varphi)} La_t^2. \quad (34)$$

The angle between the axis of Langmuir cells and the wind direction,  $\varphi$ , can be estimated from the Lagrangian shear in the upper portion of the OML, and Van Roekel et al. (2012) proposed a simple equation to obtain estimates based only on the Stokes drift profile and a log-law estimate for the Eulerian mean shear profile (which requires only knowledge of  $u_*$ ).

as a means to quantify the relative influences of wind shear and the Stokes drift on the flow, where  $u_*$  is the friction velocity in the water associated with the wind shear stress at the ocean surface  $\tau_0$ . In most LES studies,  $\tau_0$  is assumed constant in space and is related to the wind speed at a height of 10 m above the ocean surface ( $U_{10}$ ) via  $\tau_0 = C_D \rho_{air} U_{10}^2$ , where  $C_D$  is a drag coefficient.

These early works opened the door for more systematic explorations of the parameter space, with the emergence of three canonical limiting regimes: shear-driven, buoyancy-driven, and wave-driven OMLs, with the latter being the Langmuir turbulence case. Li et al. (2005) organized these three forcing mechanisms on a 2-D parameter space formed by  $La_t$  and the Hoennikker number  $Ho = 4B_0|h_e|/(U_s u_*^2)$ , where  $B_0$  is the surface buoyancy flux (defined as being positive for surface cooling that promotes convective turbulence) and  $h_e$  is the e-folding depth of the Stokes drift profile ( $h_e = -2k$  for a monochromatic wave). With a large number of LES runs, they mapped the characteristics of TKE profiles and delineated transitions between regimes. Among other conclusions, they established that ocean turbulence is dominated by Langmuir turbulence most of the time.

Belcher et al. (2012) refined the parameter space by defining velocity scales for each regime based on the mechanisms of TKE production associated with each forcing (see Figure 5). In this scheme, the velocity scales are the friction velocity  $u_*$  for shear-driven turbulence, Deardorff's velocity scale  $w_* = (B_0|h|)^{1/3}$  for buoyancy-driven turbulence (Deardorff,

Somewhat less explored is the daytime OML with surface heating, which results in a stabilizing buoyancy flux at the surface. Pearson et al. (2015) showed that the mixing promoted by Langmuir turbulence prevents the formation of a strongly stratified layer near the surface for moderate surface buoyancy fluxes. In the resulting weakly stratified OML, they found evidence that the turbulence statistics still scaled with  $w_{*L}$  and  $h$ , and that the surface buoyancy flux's main impact on the scaling is via reduction of the OML depth. However, Min and Noh (2004) showed that strong surface heating weakens Langmuir circulations, leading to their complete breakdown if heating is strong enough (characterized by  $Ho > 1$ ). This breakdown does seem to cause large effects on the turbulence characteristics. Additional studies have extended the use of LES to Langmuir turbulence in a wide range of conditions, including shallow waters (Tejada-Martinez & Grosch, 2007), Langmuir interaction with submesoscale fronts (Hamlington et al., 2014; Sullivan & McWilliams, 2018), and hurricane conditions (Sullivan et al., 2012).

One important component of LES applications to the OML still lags significantly behind their ABL counterparts, namely, the validation of LES results against field observations. This can be mostly attributed to the difficulty of obtaining detailed turbulence measurements in the OML (D'Asaro, 2014). Li et al. (2005) compared profiles of vertical velocity variance with observations obtained from a neutrally buoyant Lagrangian float presented by D'Asaro (2001), showing that LES was capable of capturing the enhancement in turbulence produced by Langmuir circulations. Kukulka et al. (2009) performed simulations of an unsteady period of growing Langmuir circulations with measurements from the SWAPP campaign presented by Smith (1992). They compared the time evolution of near-surface crosswind velocity variance with those inferred from bubble cloud observations and temperature profiles with observations from a conductivity-temperature depth instrument. Their main conclusion was that only including the vortex force the simulations were consistent with observations. Kukulka et al. (2012) showed that large-scale velocity structures observed in shallow water via acoustic Doppler profiler were also reproduced by LES. Brunner et al. (2015) compared profiles of microplastic debris with observations presented by Law et al. (2014). Chen et al. (2018) compared horizontal diffusivities obtained from LES with observations from several studies (Lawrence et al., 1995; Murthy, 1976; Okubo, 1971), as shown later in Figure 16. Overall, most of these studies argue that only by including the vortex force LES produces results that are consistent with observations. However, a robust validation of LES is still lacking.

## 4. Applications of LES to Material Transport in the OML

### 4.1. KPP and Nonlocal Fluxes

The KPP is the standard approach to parameterize vertical turbulent fluxes in large-scale ocean models that do not resolve three-dimensional turbulence. The basic framework of the KPP approach was developed for the ABL by Troen and Mahrt (1986) and adapted for the OML by Large et al. (1994). In the present context, only the vertical flux of particle mass concentration is discussed. Using the KPP framework, this flux is modeled as

$$\overline{w'C'} = -K(z) \left( \frac{\partial \bar{C}}{\partial z} - \gamma_C \right), \quad (35)$$

where  $\overline{(\cdot)}$  represents an ensemble average and  $K(z)$  is the vertical eddy diffusivity. In this model, the term  $K(z)\gamma_C$  is an additive modification to the standard eddy diffusivity approach (sometimes referred to as the nonlocal flux) introduced by Deardorff (1966) to account for the existence of fluxes in regions with very small gradients that typically occur in free convection. In KPP, the vertical eddy diffusivity is modeled as

$$K(z) = W|h| G(z/h), \quad (36)$$

where  $G(z/h) = (z/h)(1-z/h)^2$  is a polynomial (cubic) shape function,  $h < 0$  is the OML depth, and  $W$  is a velocity scale. In the original KPP,  $W$  is modeled as

$$W(z) = \frac{\kappa u_*}{\phi(z/L_o)}. \quad (37)$$

The velocity scale is capped at  $W = \kappa u_*/\phi(0.1h/L_o)$  for unstable conditions, where  $\phi(z/L_o)$  is the Monin-Obukhov similarity function (Monin & Obukhov, 1954) and  $L_o = -u_*^3/(\kappa B_0)$  is the Obukhov length scale (Obukhov, 1946; 1971). The nonlocal flux is usually modeled in terms of the surface flux of the scalar,

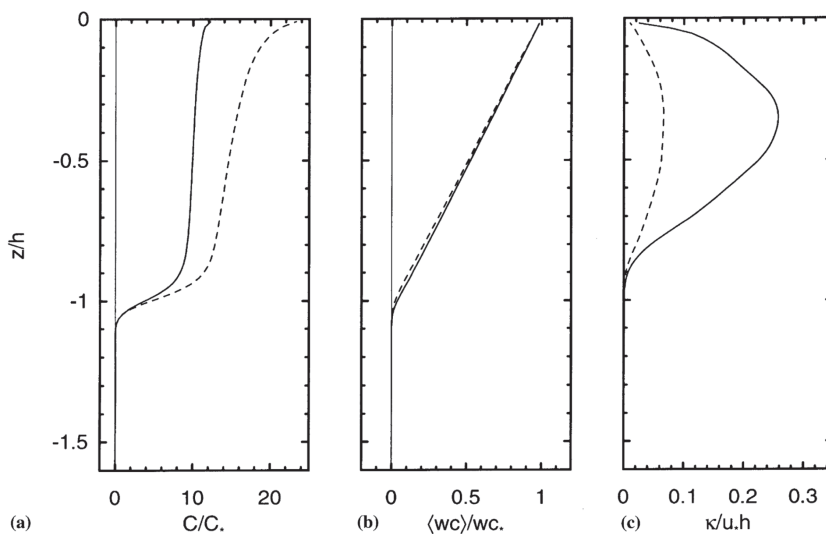


**Figure 6.** Vertical profiles of (a) mean concentration, (b) turbulent flux, and (c) eddy diffusivity for a passive tracer forced by an imposed flux at the surface in shear turbulence (dashed lines) and Langmuir turbulence (solid lines). Here  $C_* = \overline{w' C'}_0 / u_*$ , and  $w c_* = \overline{w' C'}_0$ . Reproduced from McWilliams and Sullivan (2000).

a parameterization developed for buoyancy fluxes in convective conditions that is unlikely to be generally applicable and justified for other scalars. Nevertheless, in KPP, one usually sets

$$\gamma_C = -C_\gamma \frac{\overline{w' C'}_0}{W|h|}, \quad (38)$$

where  $\overline{w' C'}_0$  is the surface flux (here we define  $\overline{w' C'}_0 > 0$  as a scalar flux out of the ocean surface). Note that in this model, the nonlocal flux would vanish for a scalar that does not have a surface flux. A more detailed description of the basic KPP framework for OML can be found in Large et al. (1994).

McWilliams and Sullivan (2000) used LES experiments with passive tracers forced at the surface and bottom of the OML (following the setup used by Wyngaard and Brost (1984) to study top-down and bottom-up transport in the convective ABL) to explore the effects of Langmuir turbulence on the eddy diffusivity, noting that Langmuir cells greatly increase the vertical mixing efficiency of tracers (see Figure 6). They proposed a modification of the original KPP by replacing the velocity scale in equation (37) with

$$W(z) = \frac{\kappa u_*}{\phi(z/L_o)} \left( 1 + \frac{C_w}{La_t^{2\alpha_w}} \right)^{\alpha_w}, \quad (39)$$

where the term in parenthesis accounts for the augmentation of the total diffusivity by Langmuir circulations. Based on their LES results, they set  $\alpha_w = 2$  and  $C_w = 0.080$ . Note that for the scalar forced at the bottom of the OML, McWilliams and Sullivan (2000) obtained larger eddy diffusivities compared to the surface forced scalar. One possible explanation is that for the bottom forced scalar, the nonlocal flux is zero (since in this case the surface flux  $\overline{w' C'}_0$  is zero), and this leads to an increase in the transport carried by the local component when compared to the scalar forced at the surface. It is possible that these differences in eddy diffusivity reflect the inadequacy of the current approach used to model nonlocal fluxes for tracers. Smyth et al. (2002) proposed an additional modification in which the constant  $C_w$  is replaced by  $C_w = f(u_*, w_*)$ .

More recently, McWilliams et al. (2012) proposed a modified profile for the eddy viscosity, which is defined based on the turbulence momentum flux and the shear in the Lagrangian velocity (as opposed to the shear in the Eulerian velocity). Yang et al. (2015) showed that this approach can be recast in terms of a correction to the traditional KPP, which can be determined a priori from estimates of the mean Lagrangian shear. Yang et al. (2015) employed this refined model (together with  $\alpha_w = 4$  and one more multiplicative function of  $La_t$  to the velocity scale) in order to allow the model to represent their LES results for oil plumes. The fact that different studies required different levels of fitting to adjust this type of parameterization to their simulation results clearly points to the need of improved, more fundamentally grounded modeling concepts.

With the goal of obtaining analytical solutions to the vertical distribution of scalar material concentration, Kukulka and Brunner (2015) and Chor et al. (2018b) developed simpler approaches to determine general velocity scales for the KPP model. Both studies neglect the nonlocal component and develop constant, bulk velocity scales. Kukulka and Brunner (2015) adopt a velocity scale given by

$$W = c_k \kappa u_*, \quad \text{with} \quad c_k = 1 + \frac{\gamma_{w1} \lambda_p}{\kappa |h|} \exp\left(-\gamma_{w2} \frac{\lambda_p}{|h|}\right). \quad (40)$$

Here  $\lambda_p$  is the peak wavelength in the wave spectrum, and the coefficients  $\gamma_{w1} = 2.49$  and  $\gamma_{w2} = 0.333$  were obtained from fits to a large number of LES runs. In this approach, the wave information enters via  $\lambda_p$ .

The approach taken by Chor et al. (2018b) is based on terms in the TKE budget. In essence, they assume the required velocity scale  $W$  to be associated to the TKE dissipation rate  $\epsilon = W^3/\ell$  and used the simplified TKE budget already employed by Belcher et al. (2012) to relate  $W$  to velocity scales for shear-, buoyancy-, and wave-driven OMLs ( $u_*$ ,  $w_*$ , and  $w_{*L}$ , respectively). This approach can be further extended based on the modifications of Langmuir number proposed by Van Roekel et al. (2012) to accommodate cases with misalignment between wind and waves, yielding

$$W^3 = u_*^3 \cos(\varphi) \left( \kappa^3 + A_L^3 La_{t,proj}^{-2} \right) + A_c^3 w_*^3. \quad (41)$$

In equation (41),  $\kappa = 0.41$  is the von Kármán constant, and  $A_L = 0.816$  and  $A_c = 1.170$  are two empirical constants defined as ratios of length scales. For the expression above to work in all cases, one must specify the angle between the axis of Langmuir cells and the wind direction  $\varphi = 0$  in the absence of surface waves. Note that this expression is consistent with the scaling  $w_{rms} \propto u_* La_t^{-2/3}$  proposed by Harcourt and D'Asaro (2008) for Langmuir turbulence with waves aligned with the wind.

One of the advantages of defining a general velocity scale encompassing all the turbulence production mechanisms is that it allows for the definition of a generalized *floatability* parameter (Chor et al., 2018b),

$$\beta = \frac{w_t}{W}, \quad (42)$$

with  $W$  given by equation (41). Based on Figure 13, we conclude that particles with  $\beta \leq 0.1$  behave approximately as tracers, while particles with  $\beta \geq 1$  behave approximately as floaters. Note that this floatability parameter can be considered as a generalization of the buoyancy-to-drift parameter  $Db = U_s/w_t$  introduced by Yang et al. (2014) in Langmuir turbulence, the parameter  $w_t/w_*$  used by Chor et al. (2018a) in buoyancy-driven turbulence, and the more commonly used ratio  $w_t/u_*$  for shear turbulence (sometimes referred to as the Rouse number in the literature on sediment transport, see Rouse, 1937). In the discussions that follow, we will refer to any of these parameters as floatability, for the sake of unifying the language. We also note that the enhancement of terminal slip velocity caused by turbulence can be accommodated by introducing an effective floatability  $\beta_{eff} = \beta + \beta_{turb}$ , where  $\beta_{turb} = (w_{t,eff} - w_t)/W$  is shown in Figure 3 (assuming that  $W$  is the appropriate velocity scale). Under these conditions, the results obtained by Good et al. (2014) indicate that for the range of TKE dissipation rates typically encountered in the OML, any phenomena controlled by floatability should have negligible impact from the effects of particle inertia (with, as already mentioned before, the possible exception of near-surface conditions with breaking waves).

Returning to the issue of nonlocal fluxes, Kukulka et al. (2012) used a passive scalar in their LES to illustrate the effects of Langmuir turbulence on mixing in shallow waters via nonlocal transport. They noted that the presence of organized flow structures in Langmuir turbulence enhanced organized vertical transport (stirring), quickly reducing vertical gradients in horizontally averaged concentration fields. However, these organized flow structures also slowed down the true irreversible mixing, in the sense that the scalar field remained organized in horizontal patches for longer times (see Figure 7).

One of the issues in studying the nonlocal fluxes using LES fields is that the separation between local and nonlocal is not straightforward. McWilliams and Sullivan (2000) separate the local and nonlocal components by assuming a KPP representation for the nonlocal flux and then adjusting the value of  $C_\gamma$  in equation (38) to maximize the smoothness in the profile of  $K(z)$ . Chen et al. (2016a) used simulations of oil plumes with

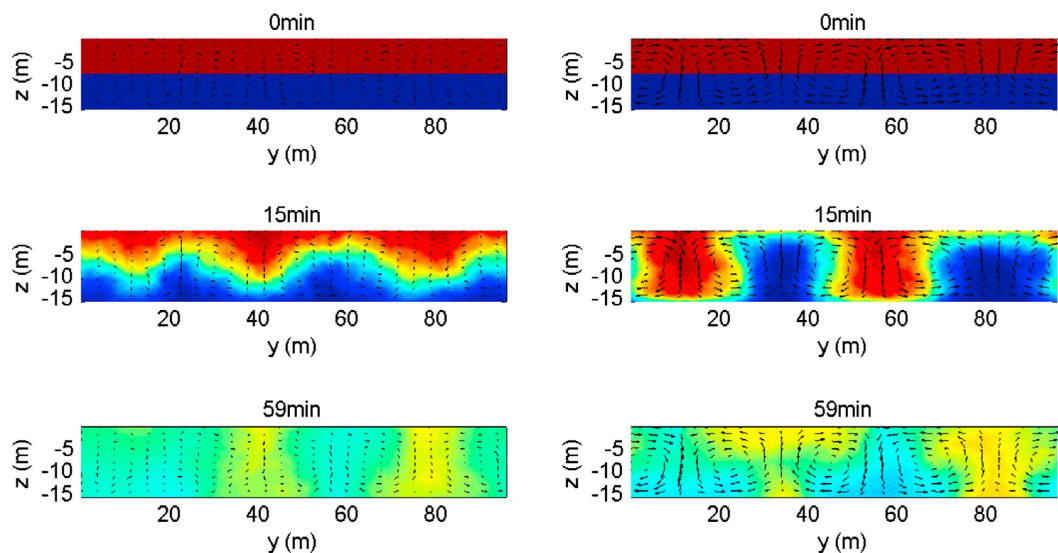


**Figure 7.** Time evolution of tracer concentration field (averaged in the cross-wind direction) for coastal ocean driven by wind shear (left panels) and Langmuir turbulence (right panels). Note that after 15 min, the tracer is well mixed in the vertical direction for the Langmuir turbulence case but the horizontal patchiness persists even after 59 min. Reproduced from Kukulka et al. (2012).

large horizontal gradients in concentration to separate local and nonlocal contributions to the total flux. The spatial structure of the concentration field allows for a range of mean vertical gradients and fluxes, assumed to be caused by the same eddy diffusivity, allowing for the determination of a spatially averaged nonlocal flux contributions. Their results show that the nonlocal fluxes contribute at least 30% of the total fluxes in Langmuir turbulence produced by swell waves. Neither approach is completely satisfactory, and new research is needed in establishing proper methods to separate local and nonlocal flux contributions.

#### 4.2. Preferential Concentration of Buoyant Material on the Surface

The term *preferential concentration* has been used in the field of turbulence to describe the behavior of inertial particles that tend to concentrate in specific regions of the flow field, leading to antidispersal of fields initially uniform (Squires & Eaton, 1991). Such phenomenon can only occur in the presence of a divergent velocity field (Balkovsky et al., 2001; Maxey, 1987). For floaters in the OML, the two-dimensional surface velocity field is itself divergent, so the preferential concentration for these particles is easily explained (see also the discussion about the importance of the gradient in the velocity divergence in Mensa et al., 2015).

In the context of the OML, Skillingstad and Denbo (1995) were the first to note that LES reproduced the concentration of floaters on the surface convergence zones, illustrating the striking differences of surface patterns between an Ekman layer with surface cooling and a Langmuir turbulence case (Figure 8). Many other early papers showed preferential concentration of floaters in Langmuir turbulence, however without quantification (McWilliams et al., 1997; McWilliams & Sullivan, 2000; Skillingstad, 2000).

Liang et al. (2012) and Kukulka et al. (2012) observed patterns for buoyant particles (gas bubbles) that were similar to those for floaters. However, buoyant particles experience the three-dimensional incompressible flow field, and the source of divergence is less obvious. Chor et al. (2018a) argues that it is the nonzero divergence of the terminal slip velocity at the surface that leads to preferential concentration of buoyant particles.

Yang et al. (2014) explored the entire range between tracers and floaters by systematically varying Stokes drift and terminal slip velocity. They defined the drift-to-buoyancy parameter  $Db = U_s/w_t$  as a measure of floatability and showed that the degree of preferential concentration was strongly correlated to  $Db$  and only marginally impacted by  $La_t$ . The authors found that the probability density functions of surface concentration for small  $Db$  were nearly Gaussian, while for large  $Db$  they had a strong peak near zero (an evidence of the voids in surface divergent regions). They used these results to explain the different visual aspects of surface oil slicks, which sometimes are clearly “fingered” and at other times appear to be more “diluted.”

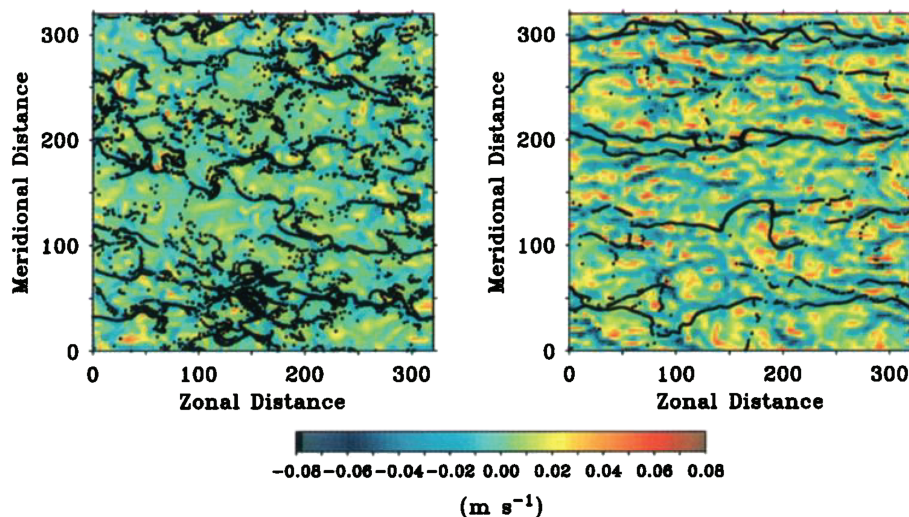


**Figure 8.** Vertical velocity 5 m below the surface (colors) for simulation driven by wind shear only (left panel) and Langmuir turbulence (right panel). Black dots mark position of floaters 1 hr after uniform release. Distances in both axes are indicated in meters. Reproduced from Skillingstad and Denbo (1995).

Mensa et al. (2015) investigated preferential concentration in free and forced convection (i.e., convection with mean shear). They noted that in free convection, floaters concentrated in regions of surface convergence displaying the classic structure of Bénard cells in a few hours and that this pattern was distorted into elongated cells by wind shear. Chor et al. (2018a) expanded on this result by investigating a wide range of particle floatability. They found that the presence of coherent vertical vortices within the vertices of some convective cells exerted a dominant effect on the preferential concentration of particles with large floatability (while for particles with low floatability this effect was negligible), as shown in Figure 9. Taylor (2018) focused on convective turbulence in the presence of a submesoscale density front and showed that the frontal downwelling is the main source of preferential concentration.

Despite the complex patterns of near-surface preferential concentration observed for buoyant materials, the ensemble averaged fields are smooth and qualitatively similar to those observed for tracers. In particular, Yang et al. (2015) showed that the mean fields for plumes originating from fairly localized sources (such as oil plumes) still displayed the same nearly Gaussian appearance of scalar plumes in turbulent fields, suggesting that simple parameterizations could be developed (Figure 10).

There is clear evidence that buoyant particles accumulate in surface convergence zones and that this effect increases in proportion to the floatability. However, at least for large floatability in convective turbulence, coherent vortices with long lifetime also play an important role. This effect of preferential concentration in downwelling regions within long-lived flow structures seems even more pronounced in submesoscale flow structures, which have much longer lifetime and sometimes comparable levels of surface convergence (D'Asaro et al., 2018; Taylor, 2018). It is not clear if this effect also exists in Langmuir turbulence, nor how the lifetime of Langmuir cells impacts surface concentration. Despite the large number of studies documenting preferential concentration of buoyant material, not many studies have focused on its implications for material transport. As discussed in section 4.5, one clear implication is a suppression of horizontal diffusion.

#### 4.3. Settling Velocity of Sinking Particles

Despite its importance, the sinking process of particles in the OML is a rather unexplored field. Noh et al. (2006) studied the effects of Langmuir turbulence (note that there was no density stratification nor a thermocline in their simulations) on the effective settling velocity of biogenic sinking particles from the OML. In their experiment, Lagrangian particles were released at the surface at an initial time, and then the effective settling velocity (defined as the mean vertical velocity of particles  $\langle w_p \rangle$ ) was determined. Results showed that the effective settling velocity is smaller than the slip velocity  $w_t$ , suggesting that turbulence reduces the rate of particle settling. Note that this cannot be related to inertial effects as discussed in section 2.2, as their model does not include particle inertia. The reduction in settling velocity is inversely proportional to  $w_t/u_*$  (see Figure 11), and this effect is more pronounced in Langmuir turbulence than in cases with wind stress

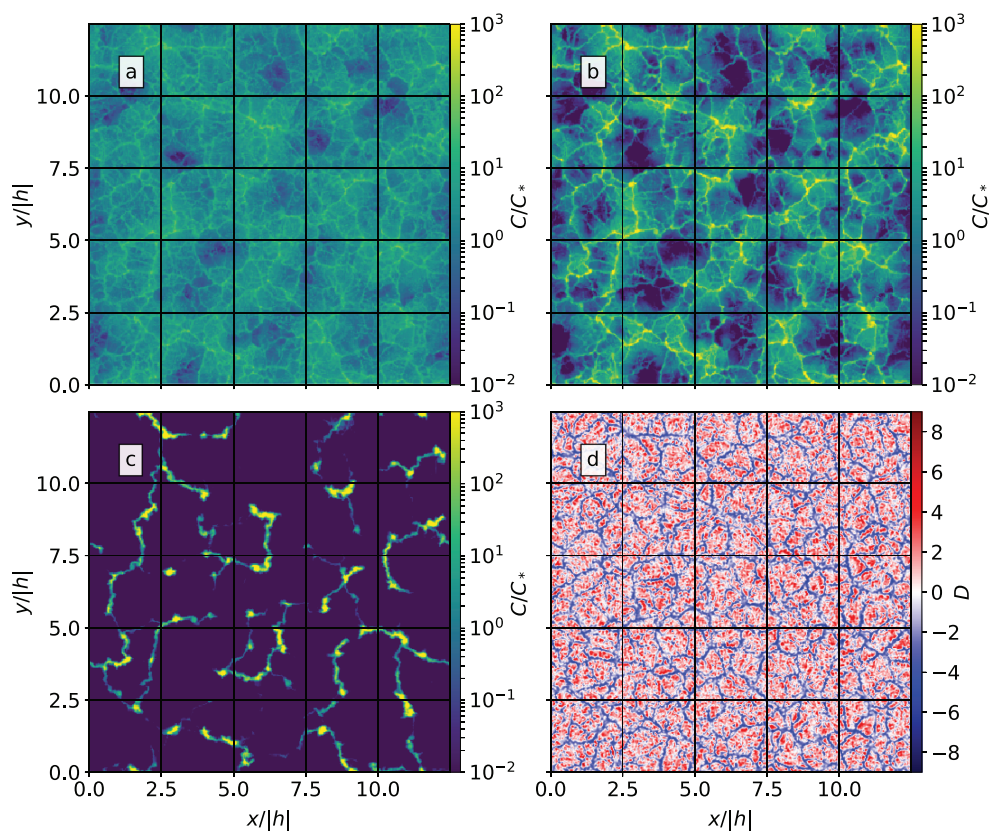


**Figure 9.** Surface concentrations for particles with (a) low, (b) intermediate, and (c) high floatability, and (d) horizontal divergence of surface velocity. Reproduced from Chor et al. (2018a).

alone. The authors interpreted this as a confirmation of the hypothesis that large vortices can significantly suppress particle settling (Stommel, 1949b).

Noh and Nakada (2010) performed a similar study for an OML in free convection and determined the sedimentation rate of particles out of the OML (i.e., the average vertical velocity of particles at the OML bottom). They observed that within the OML, particle motion is mostly determined by the large-scale convective plumes leading to mean concentration profiles that are always approximately well mixed (as expected given that all their cases have  $w_*/w_t \geq 6.0$ ). In this case, they found that the rate of sedimentation is controlled by the entrainment velocity at the bottom of the OML (i.e., the rate of deepening of the OML,  $w_e = dh/dt$ ).

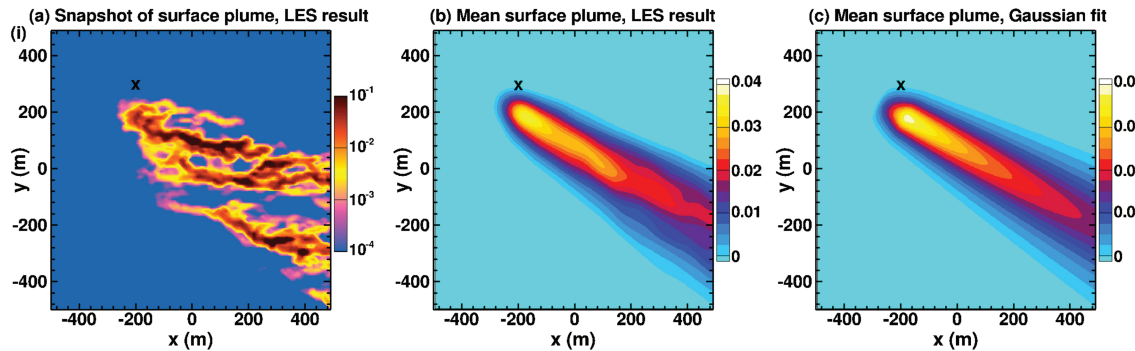


**Figure 10.** Surface concentration for particles with  $Db = 3.2$  in Langmuir turbulence: (a) instantaneous plume, (b) time-averaged plume, and (c) Gaussian fit to the time-averaged plume. Black cross symbol indicates the horizontal location of the underwater source. Reproduced from Yang et al. (2015). LES = large eddy simulation.

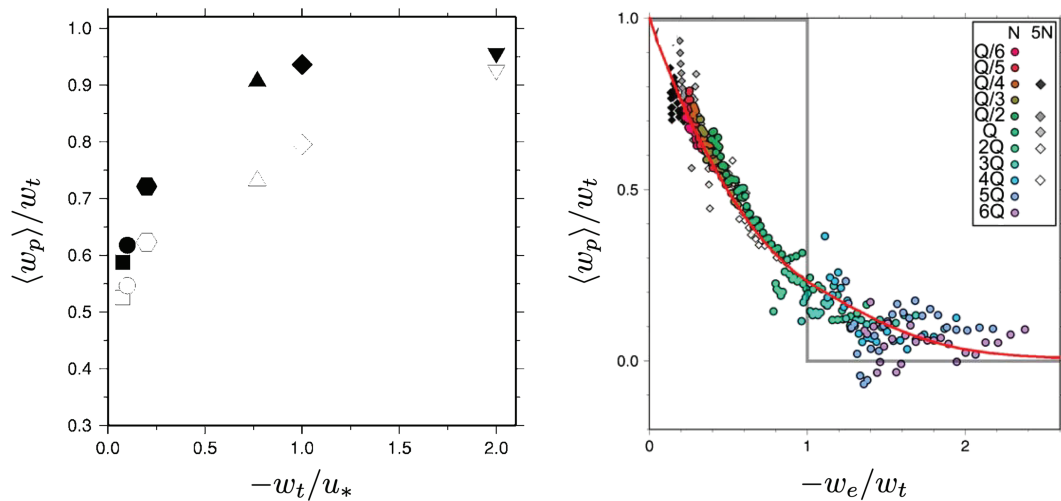


**Figure 11.** Mean vertical velocity of sinking particles in the ocean mixed layer. (Left) Comparison between shear (black symbols) and Langmuir (open symbols) turbulence. (Right) Scaling with entrainment velocity  $w_e$  for simulations of free convection (circles and diamonds indicate runs with weaker and stronger thermocline stratification, and the red line represents the fit  $\langle w_p \rangle / w_t = \exp(1.4w_e/w_t)$ ). Left panel reproduced from Noh et al. (2006) with permission from American Institute of Physics (AIP), and right panel reproduced from Noh and Nakada (2010).

Given the importance of settling particles such as phytoplankton and marine snow to a range of biogeochemical processes, the study of sinking particles certainly deserves more attention. In particular, the fact that the sinking rate does not seem to scale with the turbulence velocity scale may actually imply that in this specific problem the enhancement of settling velocity of inertial particles due to turbulence could play a significant role.

#### 4.4. Vertical Distribution of Buoyant Materials Within the OML

For the case of buoyant materials, the terminal rise velocity leads particles to concentrate in the upper portion of the OML. This effect is opposed by turbulence mixing, leading to the possibility of well-defined equilibrium concentration profiles, where both effects are balanced, which in turn can be characterized in terms of the floatability parameter. Liang et al. (2012) simulated multidispersed bubbles separated in 17 size bins between 35 µm and 10 mm using the model developed and validated by Liang et al. (2011). Equations for the different bins are coupled via gas dissolution, yielding a complex system. The overall vertical distribution in mean bubble density (including all size bins together) displays an exponential decay with depth, in agreement with observations (Crawford & Farmer, 1987). This distribution is explained by a simple balance between turbulent transport and bubble gas dissolution, without explicit inclusion of the bubble slip velocity. The formulation with an evolving size distribution, although very useful from an applied perspective, does not allow for a detailed study of the effects of floatability on the vertical profile. For an equilibrium size distribution, the authors successfully link the e-folding depth of the plume to  $w_{*L}$ . The authors also note the importance of the vertical bubble distribution (and thus turbulent mixing) on bubble-mediated air-sea gas transfer.

Yang et al. (2014) performed a systematic numerical study of the effect of floatability on vertical distribution of oil droplets in Langmuir turbulence, covering a wide range of droplet sizes and turbulent Langmuir numbers. They simulated oil plumes released from a small volume source placed below the thermocline, so that their plume is not horizontally homogeneous. They observed the effects of floatability on the vertical distribution, but no quantitative information was provided. In a follow-up study, Yang et al. (2015) quantified vertical distribution and showed that the depth of the center of mass  $h_{cm}$  scaled well as a function of  $Db$ , increasing monotonically with  $Db$ . Note that the heat flux in their simulations is small and for this case we have  $\beta \approx (A_L La_t^{4/3} Db)^{-1}$ , so all the collapses against  $Db$  can be expected to lead to collapse also with respect to the floatability parameter  $\beta$ .

Kukulka and Brunner (2015) obtained an analytical solution for the mean concentration profile of buoyant material,  $\bar{C}(z)$ , using a balance between buoyant rise and turbulent mixing with simple eddy diffusivity closures. They combined a solution with a constant eddy diffusivity  $K_0$  for the near-surface region and a

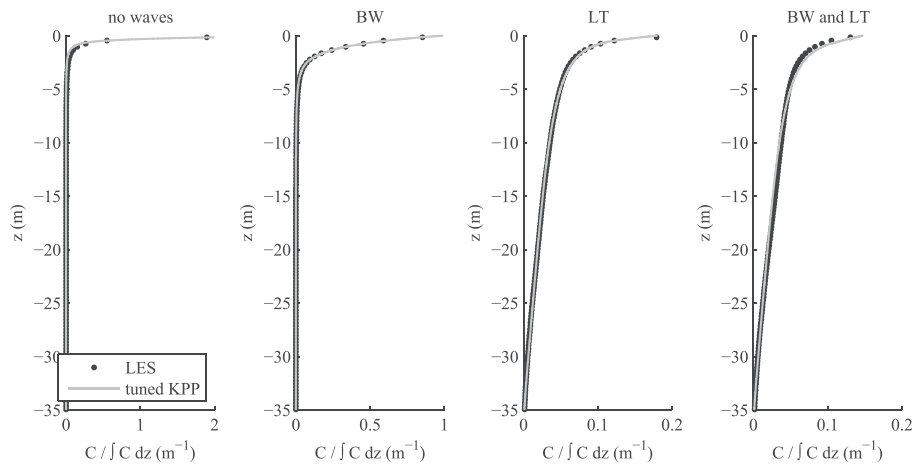


**Figure 12.** Normalized vertical profiles of mean concentration obtained from large eddy simulation (LES; symbols) and from the analytical model given by equation (43) using the parameterizations given by equations (37) and (44) for an ocean mixed layer driven by, from left to right, (i) wind shear, (ii) wind shear and breaking waves (BW), (iii) wind shear and Stokes drift (Langmuir turbulence, LT), and (iv) wind shear, breaking waves, and Stokes drift. Figure reproduced from Kukulka and Brunner (2015). KPP =  $K$ -profile parameterization.

solution based on the KPP cubic eddy diffusivity for the bulk of the OML (assuming a constant velocity scale given by equation (40) and neglecting the nonlocal flux). Their solution is given by

$$\bar{C}(z) = \begin{cases} \bar{C}(0) \exp\left(\frac{w_t z}{K_0}\right) & \text{for } z_T \leq z \\ \bar{C}(z_T) \left[ \left( \frac{1-z/h}{1-z_T/h} \right) \frac{z_T}{z} \right]^{\beta_k} \exp\left[\frac{\beta_k}{z/z_T-1} \left( \frac{z/z_T-1}{h/z_T-1} \right) \right] & \text{for } h \leq z < z_T. \end{cases} \quad (43)$$

In equation (43),  $z_T \approx -K_0/W$  is the depth where the transition between the constant eddy diffusivity and the KPP is applied,  $\beta_k = w_t/W$  is a floatability parameter, and  $W$  is the velocity scale given by equation (37). Recall that we are using  $h < 0$ . In this formulation, they used

$$\frac{K_0}{u_* |h|} = \gamma_0^{bk} \frac{z_0}{|h|} + \gamma_{01} \frac{\lambda_p}{|h|} \exp\left(-\gamma_{02} \frac{\lambda_p}{|h|}\right), \quad (44)$$

with constants  $\gamma_0^{bk} = 1.60$ ,  $\gamma_{01} = 0.145$ , and  $\gamma_{02} = 1.33$  adjusted to match LES simulations ( $z_0$  is a hydrodynamic roughness length scale). In equation (44),  $\gamma_0^{bk}$  is an enhancement factor due to breaking waves. The agreement between mean concentration profiles obtained from LES and those given by this analytical solution is quite good (see Figure 12). An important conclusion that is encoded in the fits for  $W_k$  and  $K_0$  is the fact that Langmuir turbulence impacts the eddy diffusivity within the entire OML, while breaking waves only impact the near surface diffusivity and their effect only appears in  $K_0$ . Also note that wave-breaking and Langmuir circulations are not additive effects, as the former has an important impact on the strength and organization of Langmuir circulations (Kukulka & Brunner, 2015).

Kukulka et al. (2016) used a combination of observations of buoyant microplastic marine debris and LES to show the effects of surface heating and cooling on the mean vertical distribution of material in the OML. They obtained a positive correlation between surface heating and near surface concentration, suggesting that heating reduces vertical mixing. In particular, they showed that daytime heating inhibits the vertical mixing promoted by Langmuir turbulence, as the surface stratification caused by the heating acts to suppress turbulence. They also noted that nighttime convective turbulence driven by surface cooling is too weak to mix larger particles. Their results clearly point to the need of including buoyancy in the model used to determine  $\bar{C}(z)$ .

Chor et al. (2018b) adopted the KPP eddy diffusivity for the entire OML with the velocity scale  $W$  given by equation (41). Their solution does not include wave breaking, but it accounts for the mixing promoted by surface cooling. Their solution reads

$$\bar{C}(z) = C_0 \left( \frac{1-z/h}{z/h} \right)^\beta \exp\left(\frac{-\beta}{1-z/h}\right) \quad \text{for } h \leq z \leq z_c, \quad (45)$$

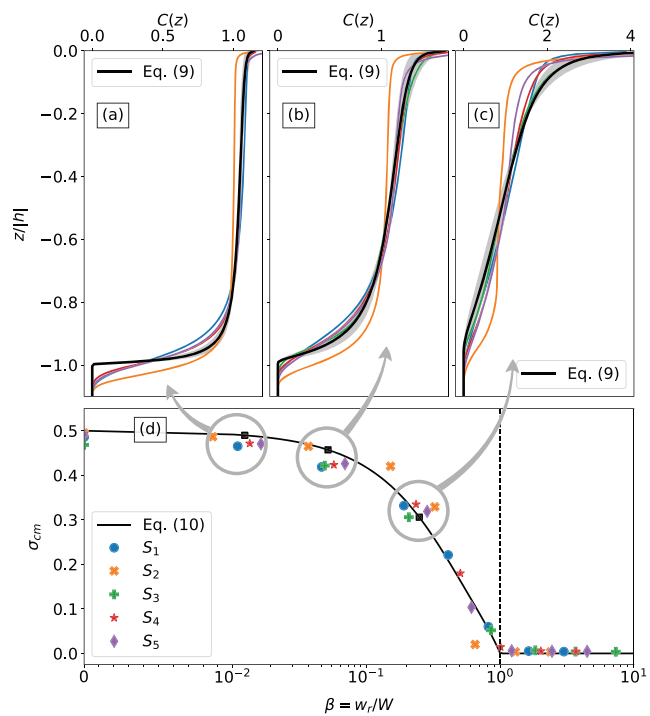


**Figure 13.** (a–c) Normalized vertical profiles of mean concentration obtained from large eddy simulation (colored lines) and from the analytical model given by equation (45) (black lines). (d) Normalized center of mass  $h_{cm}/h$  obtained from large eddy simulation (colored symbols) and approximate theoretical solution (black line). Colors indicate simulations driven by wind stress and Stokes drift (blue), buoyancy flux (orange), wind stress (green), and different combinations of wind stress, Stokes drift, and buoyancy flux (red and magenta). Figure reproduced from Chor et al. (2018b).

where  $C_0$  is a constant and  $z_c$  is a cutoff depth that marks a point where other physical processes not considered become dominant (e.g., wave breaking). In this approach, vertical mass distribution is completely determined by floatability  $\beta$ , and the agreement between profiles obtained from LES and from equation (45) is quite good for a range of OML conditions including different levels of wind shear, Stokes drift, and surface cooling (see Figure 13). This analytical solution allows to predict the center of mass, which is also in good agreement with LES (see Figure 13d) and yields a theoretical prediction for the surface trapping metric  $T_n = 1 + 2h_{cm}/h$  introduced by (Kukulka & Brunner, 2015). Note that significant wave breaking is expected to occur for winds above  $U_{10} = 5$  to 10 m/s (Banner & Peregrine, 1993). Strictly speaking, results in Figure 13 should be valid below this limit. However, results presented by Kukulka and Brunner (2015) shown in Figure 12 suggest that the effects of wave breaking to the vertical diffusivity are limited to the near surface region.

While a unified precise solution for the mean equilibrium profile of buoyant particles under all ocean conditions is still not available, most pieces are now in place. A combination of the approaches used by Kukulka et al. (2016) and Chor et al. (2018b) including wind shear, Stokes drift, breaking waves, and surface cooling seems feasible. From the results presented by Kukulka et al. (2016), it seems clear that the simplest approach to model effects of wave breaking via a near surface, constant eddy diffusivity seems satisfactory. The main missing piece is the inclusion of surface heating. This could be done by simply extending the bulk velocity scale given by equation (41) to include effects of surface heating (stabilization).

#### 4.5. Implications for Horizontal Transport and Dilution

Given the strong shear in mean speed and direction of the horizontal velocity within the OML due to planetary rotation, it should be no surprise that the vertical distribution of buoyant material strongly impacts its horizontal transport. Small vertical displacements can lead to large horizontal relative displacements. Note that even well-mixed OMLs display significant shear near the surface and near the thermocline (e.g., see hodographs in McWilliams et al., 2014, and Chen et al., 2018). The relationship between floatability and transport direction was first noted by Yang et al. (2014) in the context of surface application of dispersants

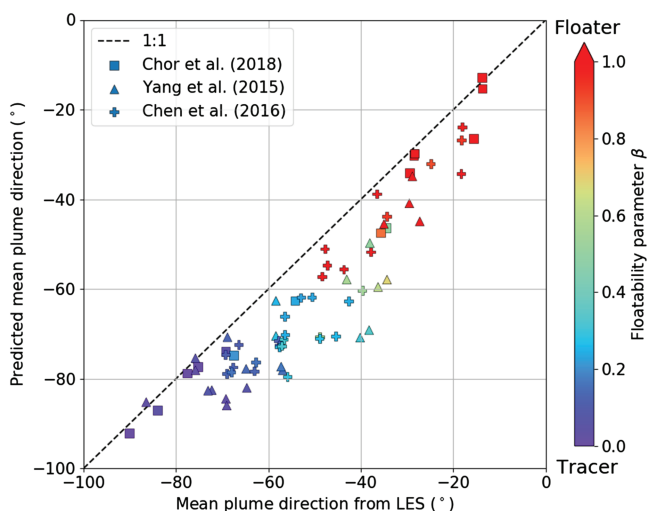


**Figure 14.** Mean transport direction for buoyant particles predicted by equation (46) displayed against results from large eddy simulation (LES) for a wide range of ocean conditions. Data from Yang et al. (2015) for Langmuir turbulence with  $0.36 \leq La_t \leq 0.61$  and a wide range of rise velocities resulting in  $0.03 \leq \beta \leq 1.37$ . Data from Chen et al. (2016a) for swell with  $La_t = 0.29$  and a wide range of angles between swell and wind covering  $360^\circ$  resulting in  $0.11 \leq \beta \leq 2.35$ . Data from Chor et al. (2018b) for several combinations of wind stress, Stokes drift, and surface buoyancy flux forcing resulting in  $0.00 \leq \beta \leq 13.4$ . Surface heating and breaking waves are not included in the analysis.

to oil plumes and later quantified in terms of  $Db$  by Yang et al. (2015). Chen et al. (2016a) documented the effects of swell on transport direction of oil droplets, and Chen et al. (2018) also noted the large changes in mean transport speed of oil plumes associated with floatability. Laxague et al. (2018) performed detailed measurements of mean velocity shear near the surface of the ocean and highlighted the potential effect on transport speed for particles with different floatability.

Chor et al. (2018b) developed a simple model to predict mean transport velocity of buoyant particles  $\mathbf{U}_h$  by neglecting horizontal transport by turbulence and using equation (45) to describe the mean concentration profile. The model is given by

$$\mathbf{U}_h = \frac{1}{|h - z_{cl}|} \int_h^{z_c} C_0 \bar{\mathbf{u}}_h(z) \left( \frac{1 - z/h}{z/h} \right)^\beta \exp \left( \frac{-\beta}{1 - z/h} \right) dz, \quad (46)$$

where  $\bar{\mathbf{u}}_h(z)$  is the mean horizontal velocity profile. The authors demonstrated good agreement between model predictions for transport speed and direction and LES results when the mean horizontal velocity profile is known. Mean model predictions are compared to LES results for a wide range of ocean conditions in Figure 14, where the mean transport direction is indicated with respect to the mean wind direction and  $\bar{\mathbf{u}}_h(z)$  from each LES simulation is used in equation (46). This result highlights the wide range of possible angles between wind and transport direction promoted by different combinations of forcings. Note that the model systematically underpredicts the angle measured in the LES, but given the range of ocean conditions included in Figure 14 (see figure caption) and the simplicity of the modeling approach, the agreement is arguably quite good. Nevertheless, more research is clearly needed in order to improve the accuracy of this type of prediction.

LES of oil plumes by Yang et al. (2014) showed that the floatability of buoyant material also had profound consequences for horizontal turbulent diffusion. In particular, they noted that plumes of oil droplets with large  $\beta$  in Langmuir turbulence did not spread much horizontally, coining the term *inhibition of dilution*. Yang et al. (2015) quantified the spreading rate of oil plumes as a function of  $Db$  and noted that larger floatability (i.e., smaller  $Db$ ) translated into slower spreading rates. Chen et al. (2018) explained this phenomenon based on the vertical distribution of buoyant materials, and the effect of the directional shear in the mean horizontal velocity on the lateral spreading rate. Liang et al. (2018) developed a full predictive theory and tied these effects of floatability on horizontal diffusion to the well-known concept of shear dispersion. In summary, the combination of vertical mixing of material and vertical shear in mean horizontal velocity dominates the horizontal diffusivity of depth-averaged buoyant material, as first demonstrated by Taylor (1953).

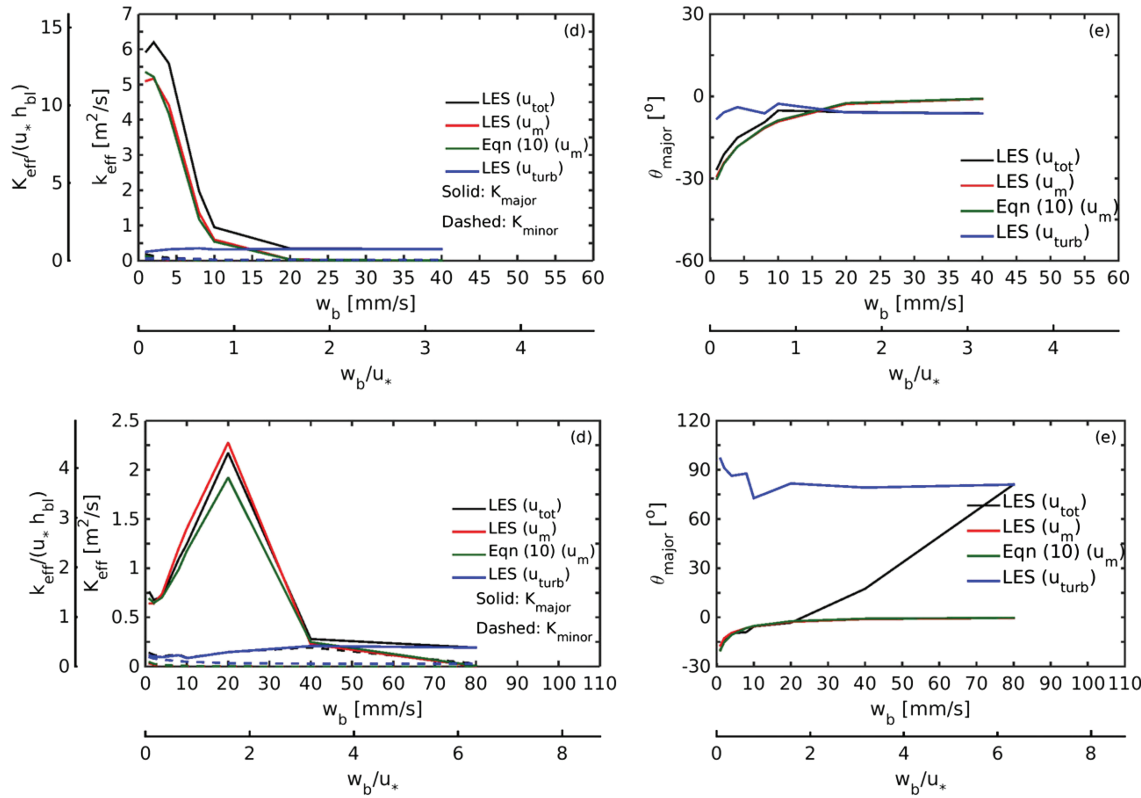


**Figure 15.** Equivalent horizontal diffusivity and axis of rotation for ocean mixed layer driven by wind shear (upper panels) and in Langmuir turbulence (lower panels) as a function of floatability parameter (here denoted as  $w_b/u_*$ ) for buoyant material. Reproduced from Liang et al. (2018). LES = large eddy simulation.

and Aris (1956) for pipe flow. Liang et al. (2018) used a recent generalization of the theory for shear dispersion developed by Esler and Ramli (2017) to write the horizontal diffusivity tensor due to the shear in the mean velocity as

$$\mathbf{K}_{h,\text{eff}} = \begin{bmatrix} -\langle(\bar{u} - \langle\bar{u}\rangle_C)M\rangle_z + \langle K_{xx}^{\text{turb}} \rangle_C & -\langle(\bar{u} - \langle\bar{u}\rangle_C)N\rangle_z + \langle K_{xy}^{\text{turb}} \rangle_C \\ -\langle(\bar{v} - \langle\bar{v}\rangle_C)M\rangle_z + \langle K_{xy}^{\text{turb}} \rangle_C & -\langle(\bar{v} - \langle\bar{v}\rangle_C)N\rangle_z + \langle K_{yy}^{\text{turb}} \rangle_C \end{bmatrix}. \quad (47)$$

In equation (47),  $\langle \cdot \rangle_z$  represents a depth-averaged quantity (within the OML) and  $\langle \cdot \rangle_C$  represents a depth-averaged quantity weighted by the vertical distribution of material  $\bar{C}(z)/\langle \bar{C} \rangle_z$ . The weighting functions  $M(z)$  and  $N(z)$  are determined based only on  $\bar{u}(z)$ ,  $\bar{v}(z)$ ,  $\bar{C}(z)$ , and  $K(z)$  (see equation 8 in Liang et al., 2018), and  $K_{xx}^{\text{turb}}$ ,  $K_{xy}^{\text{turb}}$ , and  $K_{yy}^{\text{turb}}$  are the components of horizontal turbulence diffusivity. Note that  $\mathbf{K}_{h,\text{eff}}$  is a symmetric tensor (even though this aspect is not clear in the form used in equation (47)), and it can be written in terms of principal directions and fully described by  $K_{\text{major}}$ ,  $K_{\text{minor}}$ , and  $\theta_{\text{major}}$ . These three quantities are shown in Figure 15 as a function of  $w_b/u_*$  for an OML driven by wind shear and in Langmuir turbulence. The authors concluded that for weakly buoyant material (low floatability or small  $\beta$ ), the lateral dispersion is dominated by the effects of mean shear (shear dispersion), while this effect is much weaker for highly buoyant material (high floatability or large  $\beta$ ), and turbulence dispersion is the main mechanism for horizontal spreading (see Figure 15). Liang et al. (2018) also showed that the horizontal diffusivity tensor determined using the KPP model provides a good approximation when compared to LES.

Note that the results from Chor et al. (2018b) and Liang et al. (2018) can be combined into a complete framework to predict transport and dispersion of plumes of buoyant materials in the OML for fairly general conditions (with the exception of stable stratification and breaking waves). More specifically, with the analytical expression for the mean concentration profile given by equation (45) and mean velocity profiles, mean plume transport can be estimated from equation (46), and the plume spread can be estimated from equation (47). For these calculations, mean velocity profiles can be obtained from measurements or from regional ocean models.

Another topic of interest is the effect of plume size  $\ell$  on the horizontal diffusivity  $K_h$ . According to Richardson-Obukhov's 4/3 law,  $K_h(\ell) \propto \ell^{4/3}$  (Obukhov, 1941; Richardson, 1926). This result is formally linked to the relative dispersion of fluid particles, in which the time evolution of the (ensemble) mean square distance between two fluid particles  $\sigma_D^2(t)$  is of interest. In particular, one can relate the rate of change in  $\sigma_D^2(t)$  to the space-time structure of the velocity field at scales  $\ell \propto \sigma_D$ , yielding a series of theoretical predictions for  $\sigma_D^2(t)$  and  $K_h \propto d\sigma_D^2/dt$  at different time/length scales. Theoretical predictions suggest the following regimes: (i) the Batchelor regime with  $\sigma_D^2 \propto t^2$  and  $K_h \propto \ell$  for small separations such that the solution depends on the initial separation  $\sigma_D^2(t=0)$  (Batchelor, 1952); (ii) the Richardson-Obukhov regime, with  $\sigma_D^2 \propto t^3$  and  $K_h \propto \ell^{4/3}$  for separations within the inertial subrange of turbulence; (iii) the diffusive regime with  $\sigma_D^2 \propto t$  and  $K_h \propto \ell^0 = \text{const.}$  for separations much larger than the integral scales of the flow. Clear identification of these regimes in observations and numerical simulations has been challenging because very high Reynolds numbers are required. In the OML, the strong vertical shear and consequent shear dispersion increase further the complexity of the flow, and the results from LES of the OML are not entirely conclusive either.

Mensa et al. (2015) calculated  $\sigma_D^2(t)$  for tracer particles under free-convection and forced convection (i.e., turbulence driven by a combination of surface cooling and weak wind shear). Tracer particles transported by the 3-D velocity field, as well as particles transported only by the 2-D horizontal velocity field, were used. The authors observed that  $\sigma_D^2(t)$  transitioned from an exponential growth to the Richardson-Obukhov regime in both experiments, but neither one seems to approach the asymptotic state for large  $t$ . On the other hand, simulations by Liang et al. (2018) in wind driven turbulence and Langmuir turbulence do not seem to show this signature, transitioning from the exponential growth to the ballistic regime and directly into the asymptotic  $\sigma_D^2 \propto t$  regime, bypassing the Richardson-Obukhov regime. It is possible that the simulations of Liang et al. (2018) may not have a long enough inertial subrange with Kolmogorov scaling for the emergence of the Richardson-Obukhov regime. Meanwhile, it is also well known that the energy spectrum for the large scales in free convection (and possibly in forced convection with weak winds) also presents a  $k^{-5/3}$  scaling, even though this is obviously not associated with an inertial cascade of energy (Yaglom, 1994). This particular spectral scaling in free convection could certainly lead to a Richardson-Obukhov scaling even outside of a classical inertial subrange, potentially explaining the clear Richardson-Obukhov scaling in the simulation by Mensa et al. (2015). It is also possible that the much stronger mean shear in the simulations of Liang et al. (2018) prevents the formation of the Richardson-Obukhov regime.

Empirical fits to data sets of dye dispersion (i.e., a tracer) in shallow water have yielded slightly slower increase of  $K_h$  with  $\ell$  compared to the Richardson-Obukhov regime (Lawrence et al., 1995; Murthy, 1976; Okubo, 1971; Stommel, 1949a). Lawrence et al. (1995) obtained  $K_h(\ell) = 3.2 \times 10^{-4} \ell^{1.1}$  (with  $K_h$  in  $\text{m}^2/\text{s}$  and  $\ell$  in m). It is not easy to distinguish between the two scalings in the scale-dependent horizontal diffusivities calculated by Mensa et al. (2015; see Figure 16). The clear difference in magnitude of diffusivity is likely associated with shear dispersion. Chen et al. (2018) studied the effect of chemical dispersants on oil plumes and calculated  $K_h(\ell)$  for their small oil droplet case (which has  $\beta = 0.07$ ). Their diffusivity (see Figure 16) falls exactly on top of the fit to experimental data for tracers performed by Lawrence et al. (1995). A more systematic investigation of  $\sigma_D^2(t)$  and  $K_h(\ell)$  in wide range of OML conditions is certainly needed.

#### 4.6. Applications to Plankton Dynamics

Another interesting application of LES has been on the effects of turbulence mixing on the distribution of plankton in the OML. Lewis (2005) developed a simple model of plankton dynamics by coupling three filtered advection-diffusion-reaction equations representing concentrations fields of nitrate ( $N$ ), phytoplankton ( $P$ ), and zooplankton ( $Z$ ) to an LES model of turbulent flows. In their Eulerian NPZ model, the equations are coupled to each other by processes of nitrate uptake promoting phytoplankton growth, phytoplankton grazing promoting zooplankton growth, zooplankton mortality, and recycling of nitrate due to a limitation in nitrate storage by phytoplankton and light availability. From a transport perspective, all three concentration fields are passively transported by the flow (i.e., they behave as tracer particles), and the model does not account for zooplankton swimming. Lewis et al. (2017) and Brereton et al. (2018) employed the same model to investigate the formation of peaks in biological activity in the middle of the OML and the conditions leading to horizontal patchiness in plankton populations, respectively. Both studies considered Langmuir turbulence with fixed  $Lq_r = 0.3$ , but varying wind conditions. The mid-OML peak in mean plankton concentration and the horizontal patchiness in instantaneous fluctuations appear for intermediate wind forcing (corresponding to a wind speed at 10 m of approximately  $U_{10} = 2.5 \text{ m/s}$ ), being absent in strong ( $U_{10} = 4 \text{ m/s}$ )

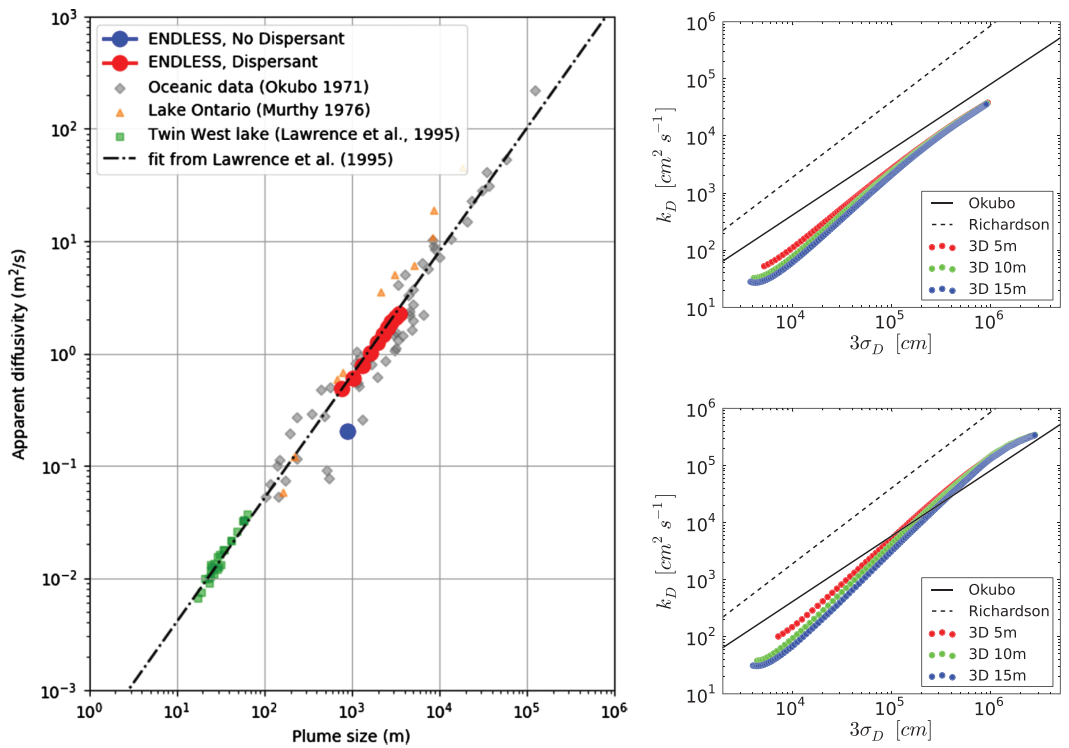


**Figure 16.** Horizontal diffusivity displayed against the scale of dispersion  $\ell$ . Left panel show large eddy simulation cases from Chen et al. (2018) with dispersant (solid red circles,  $\beta = 1.72$ ) and without dispersant (solid blue circle,  $\beta = 0.07$ ) together with observational data from dye experiments (Lawrence et al., 1995; Murthy, 1976; Okubo, 1971; Stommel, 1949a) and the empirical fit from Lawrence et al. (1995). Right panels show similar plots for the free-convection (upper panel) and forced convection (lower panel) simulations from Mensa et al. (2015) compared to the Richardson-Obukhov and the empirical fit by Okubo (1971; note that the fits by Okubo, 1971, and Lawrence et al., 1995, are nearly identical). Left panel reproduced from Chen et al. (2018), and right panels reproduced from Mensa et al. (2015). ENDLESS = Extended Nonperiodic Domain Large eddy simulation for Scalars.

and weak ( $U_{10} = 1.2$  m/s) wind conditions. Both features seem to be impacted (if not determined) by the dynamics of Langmuir-driven entrainment at the bottom of the OML. Unfortunately, the entrainment zone is not properly represented in their simulations, given the absence of a stratified thermocline below the OML and the use of a no-slip boundary condition at the bottom of the domain (which is very close to the bottom of the OML). This may impact some of the results presented by the authors. Nevertheless, the coupled LES-NPZ model is an interesting contribution, and these three studies presented a promising direction for further investigations of the coupling between dynamical processes in the OML and biological systems.

Three other studies used simpler approaches to study specific aspects of plankton dynamics. Enriquez and Taylor (2015) used an Eulerian model of phytoplankton concentration (with specified depth-dependent phytoplankton growth/death rate) to study the effects of wind stress and surface buoyancy flux on triggering spring phytoplankton blooms (in the absence of wave forcing). Smith et al. (2016) used a number of Eulerian passive tracers released at different depths to study the effects of submesoscale flows and Langmuir turbulence on vertical transport. Their results show that even in the presence of strong submesoscale eddies, Langmuir turbulence dominates the vertical transport of tracers. Finally, Smyth et al. (2017) used Lagrangian tracer particle trajectories from LES simulations of Langmuir turbulence and a model of underwater light fields to study the effects on phytoplankton photosynthetic activity in the Ross Sea Polynya.

These initial studies illustrate the potential of LES as a tool to understand plankton dynamics in the OML in response to different flow, nutrient, and light environments. Recent work with DNS using Lagrangian active particles showed important interactions between plankton gyroscopic swimming and wind driven turbulence in free-surface flows (Mashayekhpour et al., 2017). Incorporation of effects that arise from active swimmers in LES may be challenging, as most dynamical interactions are likely to be modulated by SGS dynamics and can be affected by other small-scale phenomena such as feeding currents generated by

appendage motions (Jiang et al., 2002) that would need to be parameterized in LES. Nevertheless, this is likely an important area for future research.

## 5. Open Questions and Future Directions

Since the first applications of LES to study turbulence in the OML in the mid-1990s by Skyllingstad and Denbo (1995) and McWilliams et al. (1997), numerical simulations have enabled unprecedented advances in the understanding of turbulence in the upper ocean. Moving forward, several steps are needed to further establish the credibility of LES results and the applicability of the assumptions currently being adopted in setting up the problem for LES solutions.

From a fundamental perspective, a clear assessment of the limitations of the CL equations is still lacking. Comparisons between CL theory and existing observations are encouraging (D'Asaro et al., 2014), and clearly, LES including the vortex force produces results in better agreement with observations than without it (D'Asaro, 2014). However, the use of the CL equations in turbulence-resolving simulations needs to be investigated by comparing results with those produced by wave-resolving simulations. Recent work by Wang and Özgökmen (2018) using the Reynolds-averaged Navier-Stokes equations with a constant eddy-viscosity closure showed that the Langmuir circulations produced by the CL equations and the associated vertical scalar transport correspond well to those produced by a wave-resolving model only if the unsteady interaction between currents and waves is included in the CL model. The importance of this effect in turbulence-resolving simulations is unknown. Xuan et al. (2019) performed a detailed analysis of vorticity fields in a wave-resolving LES with the surface wave form controlled by an artificial air pressure field imposed on the water surface and showed that the vorticity dynamics is consistent with the vortex force modeling in the CL equations. A clean comparison between wave-resolving simulations including two-way coupling between waves and currents and those based on the CL equations is still needed. Ideally, such comparison would be performed in more realistic settings (e.g., for broadband sea-surface wave fields) and would include analysis of turbulence statistics (at least first- and second-order moments and the components of the TKE budget).

Moving from idealized studies to more realistic oceanic conditions, studies must address the role of wave breaking and the temporal and spatial variability in Stokes drift and wind stresses. In the context of material transport, recent DNS simulations have shown that wave breaking may result in horizontal transport of fluid particles near the surface 10 times larger than that predicted by Stokes drift (Deike et al., 2017). This effect can impact the characteristics of Langmuir turbulence and significantly alter material transport in the OML, and it is currently not included in LES models. The use of a spectral wave model to determine the Stokes drift profile implemented by Sullivan et al. (2012) and Rabe et al. (2015) can certainly be used to address several limitations of current idealized LES studies (inclusion of broadband wave spectrum, incorporation of spatial and time variability of wave field, etc.). If spatial variability of wind stress on spatial scales comparable to those characteristic of OML turbulence prove to be important, a two-way coupling between atmosphere and ocean may be needed.

LES results must be validated by comparison of model outputs with observations and quantitative measurements in the ocean. Detailed observations of turbulence and material transport required for this type of model validation are not easily obtained in the OML, but they are needed to ensure that the field is moving in the correct direction. This effort should probably be accompanied by a more systematic study of the performance of different SGS models and the effects of domain size and grid resolution on the structure of OML turbulence.

One of the results of using LES to study material transport in the OML is the possibility of a unified characterization. The studies have led to the insight that characterization of relative material buoyancy is critical for which the concept of *floatability* seems to be the appropriate framework to characterize the full range of materials, from sinking particles (negative floatability) to surface floaters (infinite floatability). The floatability parameter  $\beta$  given by equation (42) with the generalized velocity scale  $W$  given by equation (41) is useful in synthesizing results from studies designed for specific sets of materials (gas bubbles, oil droplets, microplastic particles, etc.) under different sets of OML conditions associated with various ranges of wind shear, buoyancy flux, and surface wave forcings. More work is needed to further test and refine this framework and to develop extensions of the velocity scale to surface heating (stabilizing) fluxes and, possibly,

wave breaking effects. Through this framework, together with simple analytical solutions for the vertical distribution of material, horizontal transport and diffusion can be determined.

From a regional ocean modeling perspective, LES results highlight the importance of small-scale turbulence on scalar transport by larger-scale flow structures such as mesoscale and submesoscale. This effect is particularly important for buoyant particles such as gas bubbles, oil droplets, and some types of microplastic, as the vertical distribution of material within the OML has an important effect on the overall fate of these materials. Thus, an improved KPP-like approach that includes effects of Langmuir turbulence and wave breaking on the eddy diffusivity and on the nonlocal fluxes of material is needed. The recent realization that submesoscale structures significantly interact with and modulate small-scale turbulence adds another layer of complexity to this problem, suggesting the need of multiscale tools capable of accommodating the interaction between the different scales involved.

### Acknowledgments

This research was made possible by a grant from the Gulf of Mexico Research Initiative. We are thankful to Bicheng Chen for the collaboration on several papers that contributed to shaping our views on this topic and to Luke Van Roekel for suggesting the inclusion of the projected Langmuir number in the velocity scale  $W$ . M. C. is grateful to Jim McWilliams for many insightful discussions on this topic over the past few years. Original data used in Figure 14 are publicly available through the Gulf of Mexico Research Initiative Information and Data Cooperative (GRIIDC) (at <https://data.gulfresearchinitiative.org/data/R5.x283.000:0005;https://doi:10.7266/n7-sg6q-5j98>).

### References

- Aiyer, A. K., Yang, D., Chamecki, M., & Meneveau, C. (2019). A population balance model for large eddy simulation of polydisperse droplet evolution. *Journal of Fluid Mechanics*, 878, 700–739.
- Akan, C., Tejada-Martínez, A. E., Grosch, C. E., & Martinat, G. (2013). Scalar transport in large-eddy simulation of Langmuir turbulence in shallowwater. *Continental Shelf Research*, 55, 1–16.
- Andrews, D., & McIntyre, M. (1978). An exact theory of nonlinear waves on a Lagrangian-mean flow. *Journal of Fluid Mechanics*, 89(4), 609–646.
- Aris, R. (1956). On the dispersion of a solute in a fluid flowing through a tube. *Proceedings of the Royal Society of London. Series A. Mathematical and Physical Sciences*, 235(1200), 67–77.
- Auton, T., Hunt, J., & Prud'Homme, M. (1988). The force exerted on a body in inviscid unsteady non-uniform rotational flow. *Journal of Fluid Mechanics*, 197, 241–257.
- Bagheri, G., & Bonadonna, C. (2016). On the drag of freely falling non-spherical particles. *Powder Technology*, 301, 526–544.
- Balachandar, S., & Eaton, J. K. (2010). Turbulent dispersed multiphase flow. *Annual Review of Fluid Mechanics*, 42, 111–133.
- Balkovsky, E., Falkovich, G., & Foucroux, A. (2001). Intermittent distribution of inertial particles in turbulent flows. *Physical Review Letters*, 86(13), 2790.
- Banner, M., & Peregrine, D. (1993). Wave breaking in deep water. *Annual Review of Fluid Mechanics*, 25(1), 373–397.
- Batchelor, G. (1952). Diffusion in a field of homogeneous turbulence: II. The relative motion of particles. *Mathematical Proceedings of the Cambridge Philosophical Society*, 48, 345–362.
- Belcher, S. E., Grant, A. L., Hanley, K. E., Fox-Kemper, B., Van Roekel, L., Sullivan, P. P., et al. (2012). A global perspective on Langmuir turbulence in the ocean surface boundary layer. *Geophysical Research Letters*, 39, L18605. <https://doi.org/10.1029/2012GL052932>
- Berloff, P. S., McWilliams, J. C., & Bracco, A. (2002). Material transport in oceanic gyres. Part I: Phenomenology. *Journal of Physical Oceanography*, 32(3), 764–796.
- Bou-Zeid, E., Meneveau, C., & Parlange, M. (2005). A scale-dependent Lagrangian dynamic model for large eddy simulation of complex turbulent flows. *Physics of Fluids*, 17(2), 25105.
- Breivik, Ø., Janssen, P. A., & Bidlot, J.-R. (2014). Approximate Stokes drift profiles in deep water. *Journal of Physical Oceanography*, 44(9), 2433–2445.
- Brereton, A., Siddons, J., & Lewis, D. M. (2018). Large-eddy simulation of subsurface phytoplankton dynamics: An optimum condition for chlorophyll patchiness induced by Langmuir circulations. *Marine Ecology Progress Series*, 593, 15–27.
- Brunner, K., Kukulka, T., Proskurowski, G., & Law, K. (2015). Passive buoyant tracers in the ocean surface boundary layer: 2. Observations and simulations of microplastic marine debris. *Journal of Geophysical Research: Oceans*, 120, 7559–7573. <https://doi.org/10.1002/2015JC010840>
- Chelton, D. B., Gaube, P., Schlax, M. G., Early, J. J., & Samelson, R. M. (2011). The influence of nonlinear mesoscale eddies on near-surface oceanic chlorophyll. *Science*, 334(6054), 328–332.
- Chen, B., Yang, D., Meneveau, C., & Chamecki, M. (2016a). Effects of swell on transport and dispersion of oil plumes within the ocean mixed layer. *Journal of Geophysical Research: Oceans*, 121, 3564–3578. <https://doi.org/10.1002/2015JC011380>
- Chen, B., Yang, D., Meneveau, C., & Chamecki, M. (2016b). ENDLESS: An extended nonperiodic domain large-eddy simulation approach for scalar plumes. *Ocean Modelling*, 101, 121–132.
- Chen, B., Yang, D., Meneveau, C., & Chamecki, M. (2018). Numerical study of the effects of chemical dispersant on oil transport from an idealized underwater blowout. *Physical Review Fluids*, 3(8), 83801.
- Chor, T., Yang, D., Meneveau, C., & Chamecki, M. (2018a). Preferential concentration of noninertial buoyant particles in the ocean mixed layer under free convection. *Physical Review Fluids*, 3(6), 64501.
- Chor, T., Yang, D., Meneveau, C., & Chamecki, M. (2018b). A turbulence velocity scale for predicting the fate of buoyant materials in the oceanic mixed layer. *Geophysical Research Letters*, 45, 11,817–11,826. <https://doi.org/10.1029/2018GL080296>
- Coleman, S., & Vassilicos, J. (2009). A unified sweep-stick mechanism to explain particle clustering in two-and three-dimensional homogeneous, isotropic turbulence. *Physics of Fluids*, 21(11), 113301.
- Craik, A. D., & Leibovich, S. (1976). A rational model for Langmuir circulations. *Journal of Fluid Mechanics*, 73(3), 401–426.
- Crawford, G., & Farmer, D. (1987). On the spatial distribution of ocean bubbles. *Journal of Geophysical Research*, 92(C8), 8231–8243.
- Crowe, C. T., Sommerfeld, M., & Tsuji, Y. (1998). *Multiphase flows with droplets and particles*. Boca Raton: CRC press.
- D'Asaro, E. A. (2001). Turbulent vertical kinetic energy in the ocean mixed layer. *Journal of Physical Oceanography*, 31(12), 3530–3537.
- D'Asaro, E. A. (2014). Turbulence in the upper-ocean mixed layer. *Annual Review of Marine Science*, 6, 101–115.
- D'Asaro, E. A., Shcherbina, A. Y., Klymak, J. M., Molemaker, J., Novelli, G., Guigand, C. M., et al. (2018). Ocean convergence and the dispersion of flotsam. *Proceedings of the National Academy of Sciences*, 115(6), 1162–1167.
- D'Asaro, E., Thomson, J., Shcherbina, A., Harcourt, R., Cronin, M., Hemer, M., & Fox-Kemper, B. (2014). Quantifying upper ocean turbulence driven by surface waves. *Geophysical Research Letters*, 41, 102–107. <https://doi.org/10.1002/2013GL058193>
- Dean, R. G., & Dalrymple, R. A. (1991). Water wave mechanics for engineers and scientists.

- Deardorff, J. (1966). The counter-gradient heat flux in the lower atmosphere and in the laboratory. *Journal of the Atmospheric Sciences*, 23(5), 503–506.
- Deardorff, J. W. (1970a). Convective velocity and temperature scales for the unstable planetary boundary layer and for Rayleigh convection. *Journal of the atmospheric sciences*, 27(8), 1211–1213.
- Deardorff, J. W. (1970b). A numerical study of three-dimensional turbulent channel flow at large Reynolds numbers. *Journal of Fluid Mechanics*, 41(2), 453–480.
- Deardorff, J. (1973). The use of subgrid transport equations in a three-dimensional model of atmospheric turbulence. *Journal of Fluids Engineering*, 95(3), 429–438.
- Deardorff, J. W. (1980). Stratocumulus-capped mixed layers derived from a three-dimensional model. *Boundary-Layer Meteorology*, 18(4), 495–527.
- Deike, L., Pizzo, N., & Melville, W. K. (2017). Lagrangian transport by breaking surface waves. *Journal of Fluid Mechanics*, 829, 364–391.
- Denbo, D. W., & Skillingstad, E. D. (1996). An ocean large-eddy simulation model with application to deep convection in the Greenland Sea. *Journal of Geophysical Research*, 101(C1), 1095–1110.
- Donelan, M. A., Hamilton, J., & Hui, W. (1985). Directional spectra of wind-generated ocean waves. *Philosophical Transactions of the Royal Society A*, 315(1534), 509–562.
- Druzhinin, O. (1995). On the two-way interaction in two-dimensional particle-laden flows: The accumulation of particles and flow modification. *Journal of Fluid Mechanics*, 297, 49–76.
- Enriquez, R. M., & Taylor, J. R. (2015). Numerical simulations of the competition between wind-driven mixing and surface heating in triggering spring phytoplankton blooms. *ICES Journal of Marine Science*, 72(6), 1926–1941.
- Esler, J., & Ramli, H. (2017). Shear dispersion in the turbulent atmospheric boundary layer. *Quarterly Journal of the Royal Meteorological Society*, 143(705), 1721–1733.
- Ferry, J., & Balachandar, S. (2001). A fast Eulerian method for disperse two-phase flow. *International Journal of Multiphase Flow*, 27(7), 1199–1226.
- Fraga, B., & Stoesser, T. (2016). Influence of bubble size, diffuser width, and flow rate on the integral behavior of bubble plumes. *Journal of Geophysical Research: Oceans*, 121, 3887–3904. <https://doi.org/10.1002/2015JC011381>
- Germano, M. (1992). Turbulence: The filtering approach. *Journal of Fluid Mechanics*, 238, 325–336.
- Germano, M., Piomelli, U., Moin, P., & Cabot, W. H. (1991). A dynamic subgrid-scale eddy viscosity model. *Physics of Fluids A: Fluid Dynamics*, 3(7), 1760–1765.
- Good, G., Ireland, P., Bewley, G., Bodenschatz, E., Collins, L., & Warhaft, Z. (2014). Settling regimes of inertial particles in isotropic turbulence. *Journal of Fluid Mechanics*, 759, R3.
- Grooms, I., & Majda, A. J. (2013). Efficient stochastic superparameterization for geophysical turbulence. *Proceedings of the National Academy of Sciences*, 110(12), 4464–4469.
- Guseva, K., Daitche, A., Feudel, U., & Tel, T. (2016). History effects in the sedimentation of light aerosols in turbulence: The case of marine snow. *Physical Review Fluids*, 1(7), 74203.
- Hamlington, P. E., Van Roekel, L. P., Fox-Kemper, B., Julien, K., & Chini, G. P. (2014). Langmuir–submesoscale interactions: Descriptive analysis of multiscale frontal spindown simulations. *Journal of Physical Oceanography*, 44(9), 2249–2272.
- Harcourt, R. R., & D’Asaro, E. A. (2008). Large-eddy simulation of Langmuir turbulence in pure wind seas. *Journal of Physical Oceanography*, 38(7), 1542–1562.
- Hasselmann, K., Sell, W., Ross, D., & Müller, P. (1976). A parametric wave prediction model. *Journal of Physical Oceanography*, 6(2), 200–228.
- Holm, D. D. (1996). The ideal Craik-Leibovich equations. *Physica D: Nonlinear Phenomena*, 98, 415–441.
- Huang, N. E. (1979). On surface drift currents in the ocean. *Journal of Fluid Mechanics*, 91(1), 191–208.
- Huang, J., & Bou-Zeid, E. (2013). Turbulence and vertical fluxes in the stable atmospheric boundary layer. Part I: A large-eddy simulation study. *Journal of the Atmospheric Sciences*, 70(6), 1513–1527.
- Jiang, H., Meneveau, C., & Osborn, T. R. (2002). The flow field around a freely swimming copepod in steady motion. Part II: Numerical simulation. *Journal of Plankton Research*, 24(3), 191–213.
- Kaltenbach, H.-J., Gerz, T., & Schumann, U. (1994). Large-eddy simulation of homogeneous turbulence and diffusion in stably stratified shear flow. *Journal of Fluid Mechanics*, 280, 1–40.
- Kenyon, K. E. (1969). Stokes drift for random gravity waves. *Journal of Geophysical Research*, 74(28), 6991–6994.
- Khairoutdinov, M., Randall, D., & DeMott, C. (2005). Simulations of the atmospheric general circulation using a cloud-resolving model as a superparameterization of physical processes. *Journal of the Atmospheric Sciences*, 62(7), 2136–2154.
- Kukulka, T., & Brunner, K. (2015). Passive buoyant tracers in the ocean surface boundary layer: 1. Influence of equilibrium wind-waves on vertical distributions. *Journal of Geophysical Research: Oceans*, 120, 3837–3858. <https://doi.org/10.1002/2014JC010487>
- Kukulka, T., Law, K. L., & Proskurowski, G. (2016). Evidence for the influence of surface heat fluxes on turbulent mixing of microplastic marine debris. *Journal of Physical Oceanography*, 46(3), 809–815.
- Kukulka, T., Plueddemann, A. J., & Sullivan, P. P. (2012). Nonlocal transport due to Langmuir circulation in a coastal ocean. *Journal of Geophysical Research*, 117, C12007. <https://doi.org/10.1029/2012JC008340>
- Kukulka, T., Plueddemann, A. J., Trowbridge, J. H., & Sullivan, P. P. (2009). Significance of Langmuir circulation in upper ocean mixing: Comparison of observations and simulations. *Geophysical Research Letters*, 36, L10603. <https://doi.org/10.1029/2009GL037620>
- Kukulka, T., Proskurowski, G., Morét-Ferguson, S., Meyer, D., & Law, K. (2012). The effect of wind mixing on the vertical distribution of buoyant plastic debris. *Geophysical Research Letters*, 39, L07601. <https://doi.org/10.1029/2012GL051116>
- Kukulka, T., & Veron, F. (2019). Lagrangian investigation of wave-driven turbulence in the ocean surface boundary layer. *Journal of Physical Oceanography*, 49(2), 409–429.
- Large, W. G., McWilliams, J. C., & Doney, S. C. (1994). Oceanic vertical mixing: A review and a model with a nonlocal boundary layer parameterization. *Reviews of Geophysics*, 4, 363–403.
- Law, K. L., Mort-Ferguson, S. E., Goodwin, D. S., Zettler, E. R., DeForce, E., Kukulka, T., & Proskurowski, G. (2014). Distribution of surface plastic debris in the eastern Pacific Ocean from an 11-year data set. *Environmental Science & Technology*, 48(9), 4732–4738.
- Lawrence, G. A., Ashley, K. I., Yonemitsu, N., & Ellis, J. R. (1995). Natural dispersion in a small lake. *Limnology and Oceanography*, 40(8), 1519–1526. <https://doi.org/10.4319/lo.1995.40.8.1519>
- Laxague, N. J., Özgökmen, T. M., Haus, B. K., Novelli, G., Shcherbina, A., Sutherland, P., et al. (2018). Observations of near-surface current shear help describe oceanic oil and plastic transport. *Geophysical Research Letters*, 45, 245–249. <https://doi.org/10.1029/2017GL075891>
- Leibovich, S. (1977). On the evolution of the system of wind drift currents and Langmuir circulations in the ocean. Part 1. Theory and averaged current. *Journal of Fluid Mechanics*, 79(4), 715–743.

- Leibovich, S. (1980). On wave-current interaction theories of Langmuir circulations. *Journal of Fluid Mechanics*, 99(4), 715–724.
- Leibovich, S., & Radhakrishnan, K. (1977). On the evolution of the system of wind drift currents and Langmuir circulations in the ocean. Part 2. Structure of the Langmuir vortices. *Journal of Fluid Mechanics*, 80(3), 481–507.
- Leonard, A. (1975). Energy cascade in large-eddy simulations of turbulent fluid flows. *Advances in Geophysics*, 18, 237–248.
- Lesieur, M., & Metais, O. (1996). New trends in large-eddy simulations of turbulence. *Annual Review of Fluid Mechanics*, 28(1), 45–82.
- Lewis, D. (2005). A simple model of plankton population dynamics coupled with a LES of the surface mixed layer. *Journal of Theoretical Biology*, 234(4), 565–591.
- Lewis, D., Brereton, A., & Siddons, J. (2017). A large eddy simulation study of the formation of deep chlorophyll/biological maxima in un-stratified mixed layers: The roles of turbulent mixing and predation pressure. *Limnology and Oceanography*, 62(5), 2277–2307.
- Li, M., Garrett, C., & Skillingstad, E. (2005). A regime diagram for classifying turbulent large eddies in the upper ocean. *Deep Sea Research Part I: Oceanographic Research Papers*, 52(2), 259–278.
- Liang, J.-H., McWilliams, J. C., Sullivan, P. P., & Baschek, B. (2011). Modeling bubbles and dissolved gases in the ocean. *Journal of Geophysical Research*, 116, C03015. <https://doi.org/10.1029/2010JC006579>
- Liang, J.-H., McWilliams, J. C., Sullivan, P. P., & Baschek, B. (2012). Large eddy simulation of the bubbly ocean: New insights on subsurface bubble distribution and bubble-mediated gas transfer. *Journal of Geophysical Research*, 117, C04002. <https://doi.org/10.1029/2011JC007766>
- Liang, J.-H., Wan, X., Rose, K. A., Sullivan, P. P., & McWilliams, J. C. (2018). Horizontal dispersion of buoyant materials in the ocean surface boundary layer. *Journal of Physical Oceanography*, 48(9), 2103–2125.
- Lilly, D. (1967). The representation of small-scale turbulence in numerical simulation experiments, Proc. IBM Sci. Compt. Symp. Environ. Sci., White Plains, IBM, 1967.
- Lilly, D. K. (1992). A proposed modification of the Germano subgrid-scale closure method. *Physics of Fluids A: Fluid Dynamics*, 4(3), 633–635.
- Loth, E. (2008). Drag of non-spherical solid particles of regular and irregular shape. *Powder Technology*, 182(3), 342–353.
- Loth, E. (2010). Particles, drops and bubbles: Fluid dynamics and numerical methods.
- Majda, A. J. (2007). Multiscale models with moisture and systematic strategies for superparameterization. *Journal of the Atmospheric Sciences*, 64(7), 2726–2734.
- Malecha, Z., Chini, G., & Julien, K. (2014). A multiscale algorithm for simulating spatially-extended Langmuir circulation dynamics. *Journal of Computational Physics*, 271, 131–150.
- Mashayekhpour, M., Marchioli, C., Lovecchio, S., Lay, E. N., & Soldati, A. (2017). Wind effect on gyrotactic micro-organism surfacing in free-surface turbulence. *Advances in Water Resources*, 129, 328–337.
- Maxey, M. (1987). The gravitational settling of aerosol particles in homogeneous turbulence and random flow fields. *Journal of Fluid Mechanics*, 174, 441–465.
- Maxey, M. R., & Riley, J. J. (1983). Equation of motion for a small rigid sphere in a nonuniform flow. *The Physics of Fluids*, 26(4), 883–889.
- McWilliams, J. (2016). Submesoscale currents in the ocean, *Proceedings of the Royal Society A*, 472, 1–32.
- McWilliams, J. C., Huckle, E., Liang, J.-H., & Sullivan, P. P. (2012). The wavy Ekman layer: Langmuir circulations, breaking waves, and Reynolds stress. *Journal of Physical Oceanography*, 42(11), 1793–1816.
- McWilliams, J. C., Huckle, E., Liang, J., & Sullivan, P. P. (2014). Langmuir turbulence in swell. *Journal of Physical Oceanography*, 44(3), 870–890.
- McWilliams, J. C., & Restrepo, J. M. (1999). The wave-driven ocean circulation. *Journal of Physical Oceanography*, 29(10), 2523–2540.
- McWilliams, J. C., & Sullivan, P. P. (2000). Vertical mixing by Langmuir circulations. *Spill Science & Technology Bulletin*, 6(3–4), 225–237.
- McWilliams, J. C., Sullivan, P. P., & Moeng, C.-H. (1997). Langmuir turbulence in the ocean. *Journal of Fluid Mechanics*, 334, 1–30.
- Meneveau, C. (1994). Statistics of turbulence subgrid-scale stresses: Necessary conditions and experimental tests. *Physics of Fluids*, 6(2), 815–833.
- Meneveau, C. (2010). Turbulence: Subgrid-scale modeling. *Scholarpedia*, 5(1), 9489.
- Meneveau, C., & Katz, J. (2000). Scale-invariance and turbulence models for large-eddy simulation. *Annual Review of Fluid Mechanics*, 32(1), 1–32.
- Meneveau, C., Lund, T. S., & Cabot, W. H. (1996). A Lagrangian dynamic subgrid-scale model of turbulence. *Journal of Fluid Mechanics*, 319, 353–385.
- Mensa, J. A., Özgökmen, T. M., Poje, A. C., & Imberger, J. (2015). Material transport in a convective surface mixed layer under weak wind forcing. *Ocean Modelling*, 96, 226–242.
- Min, H. S., & Noh, Y. (2004). Influence of the surface heating on Langmuir circulation. *Journal of Physical Oceanography*, 34(12), 2630–2641.
- Mirocha, J., Kirkil, G., Bou-Zeid, E., Chow, F. K., & Kosović, B. (2013). Transition and equilibration of neutral atmospheric boundary layer flow in one-way nested large-eddy simulations using the weather research and forecasting model. *Monthly Weather Review*, 141(3), 918–940.
- Mitarai, S., Siegel, D., Watson, J., Dong, C., & McWilliams, J. (2009). Quantifying connectivity in the coastal ocean with application to the Southern California Bight. *Journal of Geophysical Research*, 114, C10026. <https://doi.org/10.1029/2008JC005166>
- Monin, A., & Obukhov, A. (1954). Basic laws of turbulent mixing in the atmosphere near the ground. *Tr. Akad. Nauk SSSR Geofiz. Inst.*, 24(151), 163–187.
- Murthy, C. R. (1976). Horizontal diffusion characteristics in Lake Ontario. *Journal of Physical Oceanography*, 6(1), 76–84. [https://doi.org/10.1175/1520-0485\(1976\)006<0076:hdcilo>2.0.co;2](https://doi.org/10.1175/1520-0485(1976)006<0076:hdcilo>2.0.co;2)
- Nielsen, P. (1993). Turbulence effects on the settling of suspended particles. *Journal of Sedimentary Research*, 63(5), 835–838.
- Noh, Y., Kang, I., Herold, M., & Raasch, S. (2006). Large eddy simulation of particle settling in the ocean mixed layer. *Physics of Fluids*, 18(8), 85109.
- Noh, Y., & Nakada, S. (2010). Estimation of the particle flux from the convective mixed layer by large eddy simulation. *Journal of Geophysical Research*, 115, C05007. <https://doi.org/10.1029/2009JC005669>
- Obukhov, A. (1941). On the distribution of energy in the spectrum of turbulent flow. *Bulletin of the Academy of Sciences of the USSR Geophysics*, 5, 453–466.
- Obukhov, A. (1946). Turbulence in thermally inhomogeneous atmosphere. *Trudy Inst. Teor. Geofiz. Akad. Nauk SSSR*, 1, 95–115.
- Obukhov, A. (1971). Turbulence in an atmosphere with a non-uniform temperature. *Boundary-layer meteorology*, 2(1), 7–29.
- Okubo, A. (1971). Oceanic diffusion diagrams. *Deep Sea Research and Oceanographic Abstracts*, 18, 789–802.
- Özgökmen, T. M., Poje, A. C., Fischer, P. F., Childs, H., Krishnan, H., Garth, C., et al. (2012). On multi-scale dispersion under the influence of surface mixed layer instabilities and deep flows. *Ocean Modelling*, 56, 16–30.

- Pearson, B. C., Grant, A. L., Polton, J. A., & Belcher, S. E. (2015). Langmuir turbulence and surface heating in the ocean surface boundary layer. *Journal of Physical Oceanography*, 45(12), 2897–2911.
- Pedlosky, J. (1987). *Geophysical fluid dynamics* (2nd ed.). New York: Springer. <https://books.google.com/books?id=ilbTBwAAQBAJ>
- Phillips, O. M. (1977). The dynamics of the upper ocean.
- Pierson, W. J. Jr., & Moskowitz, L. (1964). A proposed spectral form for fully developed wind seas based on the similarity theory of SA Kitagorodskii. *Journal of Geophysical Research*, 69(24), 5181–5190.
- Polton, J. A., & Belcher, S. E. (2007). Langmuir turbulence and deeply penetrating jets in an unstratified mixed layer. *Journal of Geophysical Research*, 112, C09020. <https://doi.org/10.1029/2007JC004205>
- Porté-Agel, F. (2004). A scale-dependent dynamic model for scalar transport in large-eddy simulations of the atmospheric boundary layer. *Boundary-Layer Meteorology*, 112(1), 81–105.
- Porté-Agel, F., Meneveau, C., & Parlange, M. B. (2000). A scale-dependent dynamic model for large-eddy simulation: application to a neutral atmospheric boundary layer. *Journal of Fluid Mechanics*, 415, 261–284.
- Rabe, T. J., Kukulka, T., Ginis, I., Hara, T., Reichl, B. G., D'Asaro, E. A., et al. (2015). Langmuir turbulence under Hurricane Gustav (2008). *Journal of Physical Oceanography*, 45(3), 657–677.
- Richardson, L. F. (1926). Atmospheric diffusion shown on a distance-neighbour graph. *Proceedings of the Royal Society of London. Series A, Containing Papers of a Mathematical and Physical Character*, 110(756), 709–737.
- Rouse, H. (1937). Modern conceptions of the mechanics of fluid turbulence. *Trans ASCE*, 102, 463–505.
- Sagaut, P. (2006). *Large eddy simulation for incompressible flows: An introduction*. Berlin: Springer.
- Shotorban, B., & Balachandar, S. (2007). A Eulerian model for large-eddy simulation of concentration of particles with small Stokes numbers. *Physics of Fluids*, 19(11), 118107.
- Skyllingstad, E. D. (2000). Scales of Langmuir circulation generated using a large-eddy simulation model. *Spill Science & Technology Bulletin*, 6(3–4), 239–246.
- Skyllingstad, E. D., & Denbo, D. W. (1995). An ocean large-eddy simulation of Langmuir circulations and convection in the surface mixed layer. *Journal of Geophysical Research*, 100(C5), 8501–8522.
- Smagorinsky, J. (1963). General circulation experiments with the primitive equations: I. The basic experiment. *Monthly Weather Review*, 91(3), 99–164.
- Smith, J. A. (1992). Observed growth of Langmuir circulation. *Journal of Geophysical Research*, 97(C4), 5651–5664.
- Smith, K. M., Hamlington, P. E., & Fox-Kemper, B. (2016). Effects of submesoscale turbulence on ocean tracers. *Journal of Geophysical Research: Oceans*, 121, 908–933. <https://doi.org/10.1002/2015JC011089>
- Smyth, R. L., Akan, C., Tejada-Martinez, A., & Neale, P. J. (2017). Quantifying phytoplankton productivity and photoinhibition in the Ross Sea Polynya with large eddy simulation of Langmuir circulation. *Journal of Geophysical Research: Oceans*, 122, 5545–5565. <https://doi.org/10.1002/2017JC012747>
- Smyth, W. D., Skyllingstad, E. D., Crawford, G. B., & Wijesekera, H. (2002). Nonlocal fluxes and Stokes drift effects in the K-profile parameterization. *Ocean Dynamics*, 52(3), 104–115.
- Squires, K. D., & Eaton, J. K. (1991). Preferential concentration of particles by turbulence. *Physics of Fluids A: Fluid Dynamics*, 3(5), 1169–1178.
- Stommel, H. (1949a). Horizontal diffusion due to oceanic turbulence. *Journal of Marine Research*, 8(3), 199–225.
- Stommel, H. (1949b). Trajectories of small bodies sinking slowly through convection cells. *Journal of Marine Research*, 8, 24–29.
- Sullivan, P. P., & McWilliams, J. C. (2010). Dynamics of winds and currents coupled to surface waves. *Annual Review of Fluid Mechanics*, 42, 19–42.
- Sullivan, P. P., & McWilliams, J. C. (2018). Frontogenesis and frontal arrest of a dense filament in the oceanic surface boundary layer. *Journal of Fluid Mechanics*, 837, 341–380.
- Sullivan, P. P., McWilliams, J. C., & Melville, W. K. (2007). Surface gravity wave effects in the oceanic boundary layer: Large-eddy simulation with vortex force and stochastic breakers. *Journal of Fluid Mechanics*, 593, 405–452.
- Sullivan, P. P., McWilliams, J. C., & Moeng, C.-H. (1994). A subgrid-scale model for large-eddy simulation of planetary boundary-layer flows. *Boundary-Layer Meteorology*, 71(3), 247–276.
- Sullivan, P. P., Romero, L., McWilliams, J. C., & Melville, W. K. (2012). Transient evolution of Langmuir turbulence in ocean boundary layers driven by hurricane winds and waves. *Journal of Physical Oceanography*, 42(11), 1959–1980.
- Taylor, G. I. (1953). Dispersion of soluble matter in solvent flowing slowly through a tube. *Proceedings of the Royal Society of London. Series A. Mathematical and Physical Sciences*, 219(1137), 186–203.
- Taylor, J. R. (2018). Accumulation and subduction of buoyant material at submesoscale fronts. *Journal of Physical Oceanography*, 48(6), 1233–1241.
- Teixeira, M. A. C., & Belcher, S. E. (2010). On the structure of Langmuir turbulence. *Ocean Modelling*, 31, 105–119.
- Tejada-Martinez, A., & Grosch, C. (2007). Langmuir turbulence in shallow water. Part 2. Large-eddy simulation. *Journal of Fluid Mechanics*, 576, 63–108.
- Thomson, D. (1987). Criteria for the selection of stochastic models of particle trajectories in turbulent flows. *Journal of Fluid Mechanics*, 180, 529–556.
- Tolman, H. L. (2009). User manual and system documentation of WAVEWATCH III TM version 3.14. *Technical Note, MMAB Contribution*, 276, 220.
- Troen, I., & Mahrt, L. (1986). A simple model of the atmospheric boundary layer; sensitivity to surface evaporation. *Boundary-Layer Meteorology*, 37(1–2), 129–148.
- Van Roekel, L., Fox-Kemper, B., Sullivan, P., Hamlington, P., & Haney, S. (2012). The form and orientation of Langmuir cells for misaligned winds and waves. *Journal of Geophysical Research*, 117, C05001. <https://doi.org/10.1029/2011JC007516>
- van den Bremer, T. S., & Breivik, Ø. (2018). Stokes drift. *Philosophical Transactions. Series A, Mathematical, physical, and engineering sciences*, 376, 2111.
- Wang, L.-P., & Maxey, M. R. (1993). Settling velocity and concentration distribution of heavy particles in homogeneous isotropic turbulence. *Journal of Fluid Mechanics*, 256, 27–68.
- Wang, P., & Özgökmen, T. (2018). Langmuir circulation with explicit surface waves from moving-mesh modeling. *Geophysical Research Letters*, 45, 216–226. <https://doi.org/10.1029/2017GL076009>
- Webb, A., & Fox-Kemper, B. (2011). Wave spectral moments and Stokes drift estimation. *Ocean Modelling*, 40(3–4), 273–288.
- Weil, J. C., Sullivan, P. P., & Moeng, C.-H. (2004). The use of large-eddy simulations in Lagrangian particle dispersion models. *Journal of the Atmospheric Sciences*, 61(23), 2877–2887.

- Woolf, D. K., & Thorpe, S. (1991). Bubbles and the air-sea exchange of gases in near-saturation conditions. *Journal of Marine Research*, 49(3), 435–466.
- Wyngaard, J. C., & Brost, R. A. (1984). Top-down and bottom-up diffusion of a scalar in the convective boundary layer. *Journal of the Atmospheric Sciences*, 41(1), 102–112.
- Xuan, A., Deng, B.-Q., & Shen, L. (2019). Study of wave effect on vorticity in Langmuir turbulence using wave-phase-resolved large-eddy simulation. *Journal of Fluid Mechanics*, 875, 173–224.
- Yaglom, A. (1994). Fluctuation spectra and variances in convective turbulent boundary layers: A reevaluation of old models. *Physics of Fluids*, 6(2), 962–972.
- Yang, D., Chamecki, M., & Meneveau, C. (2014). Inhibition of oil plume dilution in Langmuir ocean circulation. *Geophysical Research Letters*, 41, 1632–1638. <https://doi.org/10.1002/2014GL059284>
- Yang, D., Chen, B., Chamecki, M., & Meneveau, C. (2015). Oil plumes and dispersion in Langmuir, upper-ocean turbulence: Large-eddy simulations and K-profile parameterization. *Journal of Geophysical Research: Oceans*, 120, 4729–4759. <https://doi.org/10.1002/2014JC010542>
- Yang, D., Chen, B., Socolofsky, S. A., Chamecki, M., & Meneveau, C. (2016). Large-eddy simulation and parameterization of buoyant plume dynamics in stratified flow. *Journal of Fluid Mechanics*, 794, 798–833.
- Zhang, Z., Wang, W., & Qiu, B. (2014). Oceanic mass transport by mesoscale eddies. *Science*, 345(6194), 322–324.
- Zheng, L., & Yapa, P. D. (2000). Buoyant velocity of spherical and nonspherical bubbles/droplets. *Journal of Hydraulic Engineering*, 126(11), 852–854.